



A Class of Fluid-Structure Interaction Problems with Analytical Solutions for the Validation of Numerical Methods

Yongxing Wang and Olivier Pironneau

Communicated by A. Quarteroni

Abstract. Analytical solutions to Fluid-Structure Interaction (FSI) problems are almost absent in the literature. However, they are crucial for validation and convergence analysis of numerical methods, as well as for providing insight into the complex coupling dynamics between fluids and solids. In this paper, we derive two analytical and one semi-analytical solutions for three FSI problems, spanning a class of solutions by varying their geometrical and physical parameters. All solutions exhibit complex nonlinear behaviours, which we compare with numerical simulations using a monolithic method. These three FSI problems are described in the cylindrical coordinates, drawing inspiration from Couette flow, with two of them featuring a moving fluid-solid interface and the third incorporating a nonlinear constitutive solid model. To the best of our knowledge, for the first time, we present FSI problems with analytical solutions that include a moving interface.

Keywords. Fluid-structure interaction, Analytical solution, Finite element, Monolithic method, One-velocity field.

1. Introduction

Fluid-Structure Interaction (FSI) problems are prevalent across various fields, including aerodynamics [3, 5, 27], biomedical science [4, 5, 25], ocean dynamics [1, 13, 17], and so on. For most FSI problems, analytical solutions to the governing equations are intractable, and numerical simulations play a crucial role in elucidating the fundamental physics underlying the complex coupling between fluids and structures.

1.1. A Brief Summary of Numerical Methods for Fluid-Structure Interactions

Numerical methods for FSI problems have rapidly advanced over recent decades. Classical partitioned or segregated methods have been prominent over the past two decades, which represent some of the earliest numerical approaches developed for FSI problems and are still evolving, particularly in terms of parallelisation [29, 43], efficiency [20, 33], stability, accuracy [11], and adaptivity [2, 10, 11]. Monolithic methods solve the fluid and solid equations within a single equation system. This approach has gained widespread acceptance as a more robust numerical method compared to classic partitioned methods.

Monolithic FSI methods were initially developed using an Arbitrary Lagrangian–Eulerian (ALE) interface-fitted mesh, solving for fluid velocity, pressure, and solid displacement, with continuity enforced via a Lagrange multiplier [23, 25, 26]. Recently, these methods have been developed to use a background Cartesian mesh with locally cut elements, known as the locally modified FEM [12, 18], or use two meshes [8, 28], together with the distributed Lagrange multipliers to enforce velocity continuity. Alternatively, fully Eulerian methods [16, 31, 32, 35, 41] solve the FSI system over a fixed mesh, using an indicator function and an Initial Points (IP) set to track the interface.

We have recently developed a one-velocity monolithic method that solves for a unified velocity field across the entire domain. It can use a single interface-fitted mesh [15, 22, 39] or two meshes with isoparametric interpolation to ensure interface consistency [36–38]. This paper benchmarks our one-velocity method against three (semi-)analytical FSI problems introduced herein.

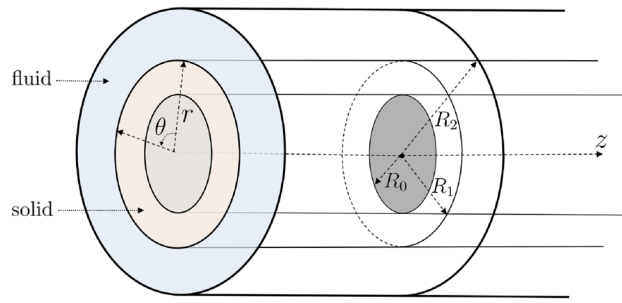


FIG. 1. FSI diagram of an elastic solid and viscous fluid between concentric cylinders (R_0 and R_2), with the middle cylinder being a fixed-rod

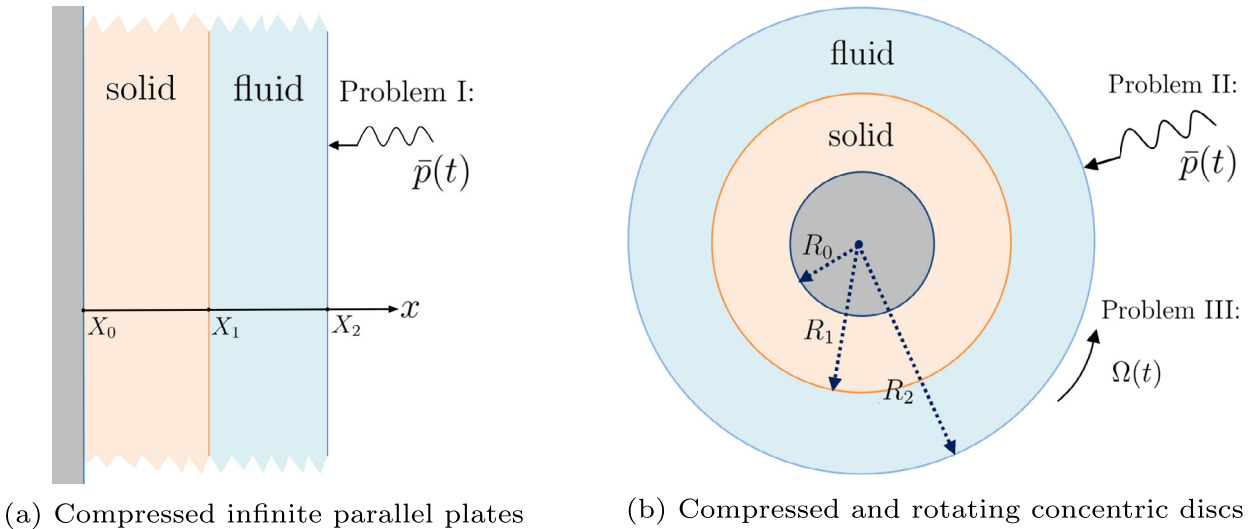
1.2. Analytical Solutions in Special Computational Domains

Analytical solutions to the Navier-Stokes equation may only be obtained for simple geometries with additional assumptions, utilising symmetry to reduce the equation to lower dimensions, such as the Couette flow between two concentric cylinders [34, 40], or the pulsatile flow in a pipe [42]. Both the Couette flow and the pulsatile flow can be modelled in a cylindrical coordinate system: $r - \theta - z$ are radial, circumferential, and axial coordinates respectively as shown in Figure 1; exploring the symmetry, the former may be reduced to a problem on $r - \theta$ plane while the latter on $r - z$ plane. Additional assumptions of the velocity profiles of the Couette and the pulsatile flow can further reduce them to one-dimensional problems, which may be solved analytically.

Analytical solutions of FSI problems, where Navier-Stokes equations are coupled with solid equations, have rarely been studied, although there are linearised FSI problems being studied to analyse the added-mass effect [9, 14]. Building on the Couette and pulsatile fluid flow, analytical FSI problems may be created to fill this gap in the FSI community. In a recent study [24], analytical solutions of the pulsatile flow in an elastic pipe have been derived, which is reduced to a one-dimensional ODE based on the assumption that the fluid velocity and solid displacement are axisymmetric and axially invariant – reduced to a 2D problem on $r - z$ plane, which only have the axial components. In this paper, we consider the Couette flow around an elastic solid as shown in Figure 1, and also assume that the fluid velocity and solid displacement are axisymmetric and axially invariant – reduced to a 2D problem on $r - \theta$ plane. However, depending on the boundary conditions, the velocity and displacement fields have either the radial or circumferential component: Problem II and III respectively in Figure 2 (b). Similar to Couette flow between two parallel plates, we will also consider an FSI problem between two parallel plates (Problem I), using a pressure boundary condition, as shown in Figure 2 (a). Notice that it is also possible to consider an analytical FSI problem by applying a shearing boundary condition to the parallel plates in Figure 2 (a), in which case both the velocity and displacement fields only have components in the vertical direction. However, we do not consider this case, as a similar scenario has already been studied in [24], albeit with pulsatile-flow boundary conditions applied at the inlet and outlet.

The complexities of the three problems are as follows: in Problems I and II, the application of normal stress induces a moving interface, increasing the overall difficulty. Furthermore, the solid constitutive equations are formulated in the reference configuration, while the fluid equations are expressed in the current configuration, introducing additional challenges due to this inconsistency. In contrast, the primary complexity in Problem III stems from the nonlinear solid constitutive model.

The rest of this paper is organised as follows: the Partial Differential Equations (PDEs) of the FSI problems are introduced in Section 2, followed by a discussion of the three FSI problems in Sections 3, 4, and 5 respectively. In each of these sections, the FSI problem is described first, followed by a detailed analysis and derivation of its analytical solution, with numerical validation provided finally. Conclusions are drawn in Section 6.



(a) Compressed infinite parallel plates

(b) Compressed and rotating concentric discs

FIG. 2. In problem I and II, a periodic normal stress is enforced at outer fluid boundary, compressing the solids due to the compression of the fluids. In problem III, a periodic angular velocity is prescribed at the outer boundary of the fluid, causing the solid disc to rotate forward and backward due to the rotation of the fluid

2. FSI Equations

In this section, we introduce the PDEs for the three fluid-structure interaction problems as illustrated in Figure 2. For the first two cases, a periodic normal force is prescribed at the outer boundary of the fluid, as depicted, causing the solid to be propelled by the fluid and move along the normal/radial direction. For the third case, a periodic velocity is prescribed at the outer boundary of the fluid along the circumferential direction, leading to the solid being dragged to rotate forward and backward.

An incompressible Newtonian fluid is utilised for all the three problems in this paper, described as:

$$\rho^f \dot{\mathbf{u}} = \mu^f \nabla \cdot \nabla \mathbf{u} - \nabla p^f, \quad (1)$$

$$\nabla \cdot \mathbf{u} = 0, \quad (2)$$

where ρ^f and μ^f represent the fluid density and viscosity, respectively, \mathbf{u} denotes the velocity vector, and p^f denotes the pressure. $\dot{\mathbf{u}} = \frac{d}{dt} \mathbf{u} = \partial_t \mathbf{u} + \mathbf{u} \cdot \nabla \mathbf{u}$ is the total derivative of time.

Two solid models are considered in this paper. In problem I and II, we employ a compressible linear elastic solid described in the reference configuration:

$$\rho^s \ddot{\mathbf{d}} = \mu^s \hat{\nabla} \cdot (\hat{\nabla}^\top \mathbf{d} + \hat{\nabla} \mathbf{d}) + \lambda^s \hat{\nabla}(\hat{\nabla} \cdot \mathbf{d}), \quad (3)$$

where μ^s and λ^s are the Lamé constants, ρ^s is the solid density, and \mathbf{d} is the displacement vector. In problem III, we use an incompressible hyperelastic neo-Hookean model described in the current configuration:

$$\rho^s \ddot{\mathbf{d}} = \mu^s \nabla \cdot (\mathbf{F} \mathbf{F}^\top - \mathbf{I}) - \nabla p^s. \quad (4)$$

In the above equations (3) and (4), $\ddot{\mathbf{d}} = \frac{d^2 \mathbf{d}}{dt^2}$ denotes the second-order material derivative with respect to time; \mathbf{I} is the identity tensor; $\mathbf{F} = \partial_{\mathbf{x}} \mathbf{d} + \mathbf{I}$ is the deformation gradient tensor, where $\partial_{\mathbf{x}}$ denotes the derivative with respect to the reference configuration; and p^s denotes the pressure in the incompressible solid model. The FSI system can be closed by appropriate boundary and initial conditions. As shown in the Figure 2, we shall use a wall-boundary at X_0 or R_0 for all the three problems. At the outer fluid boundary, either a normal stress (Problem I and II) or a tangential velocity profile is prescribed. At the fluid-solid interface (X_1 or R_1), the continuity of the velocity and the continuity of the normal stress are

applied. We shall discuss details of these boundary conditions, as well as the initial conditions, separately for the three specific problems in the following sections.

In the above, ∇ and $\hat{\nabla}$ represent the gradient operator in the current and reference configurations respectively. Equations (1) to (3) do not specify a coordinate system. In the Cartesian coordinate system, we use $X\mathbf{i} + Y\mathbf{j}$ to denote a vector in the reference configuration, and $x\mathbf{i} + y\mathbf{j}$ to denote a vector in the current configuration, with $\mathbf{i} = (1, 0)^\top$ and $\mathbf{j} = (0, 1)^\top$ being the basis vectors. In the polar coordinate system, we use $r\mathbf{e}_r$ and $R\hat{\mathbf{e}}_r$ to represent vectors in the current and reference configurations respectively. The polar basis vectors $\mathbf{e}_r - \mathbf{e}_\theta$ (or $\hat{\mathbf{e}}_r - \hat{\mathbf{e}}_\theta$) are functions of θ (or $\hat{\theta}$) and can be derived as follows: since $(x, y) = (r \cos \theta, r \sin \theta)$,

$$\mathbf{e}_r = \frac{\partial_r(x, y)}{|\partial_r(x, y)|} = (\cos \theta, \sin \theta)^\top, \quad (5)$$

$$\mathbf{e}_\theta = \frac{\partial_\theta(x, y)}{|\partial_\theta(x, y)|} = (-\sin \theta, \cos \theta)^\top. \quad (6)$$

Similarly, $\hat{\mathbf{e}}_r = (\cos \hat{\theta}, \sin \hat{\theta})^\top$ and $\hat{\mathbf{e}}_\theta = (-\sin \hat{\theta}, \cos \hat{\theta})^\top$. The relation between $(\mathbf{e}_r, \mathbf{e}_\theta)$ and $(\hat{\mathbf{e}}_r, \hat{\mathbf{e}}_\theta)$ is given by:

$$\hat{\mathbf{e}}_r = \cos \alpha \mathbf{e}_r - \sin \alpha \mathbf{e}_\theta, \quad \hat{\mathbf{e}}_\theta = \sin \alpha \mathbf{e}_r + \cos \alpha \mathbf{e}_\theta, \quad (7)$$

where $\alpha = \theta - \hat{\theta}$ is the angular displacement. The relationship of the bases between these two coordinate systems is described as:

$$(\mathbf{e}_r, \mathbf{e}_\theta) \mathbf{Q} = (\mathbf{i}, \mathbf{j}), \quad (8)$$

where

$$\mathbf{Q} = \begin{pmatrix} \cos \theta & \sin \theta \\ -\sin \theta & \cos \theta \end{pmatrix}. \quad (9)$$

With the above notations, it is straightforward to compute the Jacobian matrix:

$$\mathbf{J} = \partial_{(r, \theta)}(x, y) = \begin{pmatrix} \cos \theta & \sin \theta \\ -r \sin \theta & r \cos \theta \end{pmatrix}, \quad (10)$$

and its inverse

$$\mathbf{J}^{-1} = \partial_{(x, y)}(r, \theta) = \frac{1}{r} \begin{pmatrix} r \cos \theta & -\sin \theta \\ r \sin \theta & \cos \theta \end{pmatrix}, \quad (11)$$

and further the gradient operator in the polar coordinate system:

$$\begin{aligned} \nabla &= (\mathbf{i}, \mathbf{j}) \partial_{(x, y)} = (\mathbf{e}_r, \mathbf{e}_\theta) \mathbf{Q} \mathbf{J}^{-1} \partial_{(r, \theta)} \\ &= \left(\mathbf{e}_r, \frac{\mathbf{e}_\theta}{r} \right) \partial_{(r, \theta)} = \mathbf{e}_r \partial_r + \mathbf{e}_\theta \frac{1}{r} \partial_\theta. \end{aligned} \quad (12)$$

The gradient operator is a first-order tensor. The derivative of the polar basis:

$$\begin{pmatrix} \partial_r \mathbf{e}_r & \partial_r \mathbf{e}_\theta \\ \partial_\theta \mathbf{e}_r & \partial_\theta \mathbf{e}_\theta \end{pmatrix} = \begin{pmatrix} 0 & 0 \\ \mathbf{e}_\theta & -\mathbf{e}_r \end{pmatrix} = \mathbf{e}_\theta (\mathbf{e}_r \mathbf{e}_\theta) - \mathbf{e}_r (\mathbf{e}_\theta \mathbf{e}_\theta) \quad (13)$$

will also be used to derive the control equations in the following sections, which is a second-order tensor, with basis $\mathbf{e}_r \mathbf{e}_\theta$ being $\mathbf{e}_r \otimes \mathbf{e}_\theta$ for short, etc. We can further compute the dot product of two gradient operators which is a scalar:

$$\begin{aligned} \nabla \cdot \nabla &= \left(\mathbf{e}_r \partial_r + \mathbf{e}_\theta \frac{1}{r} \partial_\theta \right) \cdot \left(\mathbf{e}_r \partial_r + \mathbf{e}_\theta \frac{1}{r} \partial_\theta \right) \\ &= \partial_{rr} + \frac{1}{r} \partial_r + \frac{1}{r^2} \partial_{\theta\theta}. \end{aligned} \quad (14)$$

Notice that the operators in (12), (13), and (14) take the same form in the reference coordinate system.

3. Problem I: Compressed Parallel Plates

For the computational geometry and normal-force boundary condition shown in Figure 2 (a), we assume that only the horizontal velocity component u is non-zero, which, together with the pressure p , depends only on x and t . The fluid equations (1) and (2) then reduce to one-dimensional PDEs as follows:

$$\rho_f \dot{u}(x, t) = -p'(x, t), \quad (15)$$

$$u'(x, t) = 0, \quad (16)$$

Similarly, we assume the solid displacement only has the horizontal component d , which is a function of X and t . Then the solid equation (3) reduces to

$$\rho^s \ddot{d}(X, t) = (2\mu^s + \lambda^s) d''(X, t). \quad (17)$$

The fluid equation (15) is expressed in the current or physical domain corresponding to the reference domain $[X_1, X_2]$, while the solid (17) equation is expressed directly in the reference domain $[X_0, X_1]$. We use the Lagrangian mapping to find the current domain for the fluid, i.e., extending the solid displacement $d(X, t)$ ($X \in [X_0, X_1]$) to the displacement of the fluid particles $\xi(X, t)$ ($X \in [X_1, X_2]$), with $\xi(X_1, t) = d(X_1, t)$ at the interface. Let $x_1(t) = X_1 + \xi(X_1, t)$ and $x_2(t) = X_2 + \xi(X_2, t)$, then $x(X, t) = X + \xi(X, t)$ with $X \in [X_1, X_2]$ represents a general point in the current domain $[x_1(t), x_2(t)]$.

The FSI system is completed with the following boundary conditions:

$$d(X_0, t) = 0, \quad (18)$$

$$\dot{d}(X_1, t) = u(x_1(t), t), \quad (19)$$

$$(2\mu^s + \lambda^s) d'(X_1, t) = -p(x_1(t), t), \quad (20)$$

$$p(x_2(t), t) = \bar{p}(t). \quad (21)$$

3.1. Analytical Solution

With $\omega = \phi \sqrt{(2\mu^s + \lambda^s)/\rho^s}$,

$$d(X, t) = \frac{a}{\omega} \sin(\phi(X - X_0)) \sin(\omega t), \quad (22)$$

is the general solution of (17), which also satisfies the homogeneous boundary condition (18) and initial condition $d(X, 0) = 0$.

$$\dot{d}(X_1, t) = a \sin(\phi(X_1 - X_0)) \cos(\omega t) \quad (23)$$

is the velocity at the interface and also equivalent to the fluid velocity, $u(x, t)$, across the fluid domain $[X_1, X_2]$, since (16): $u'(x, t) = 0 \Rightarrow u(x, t)$ is constant in x . Therefore, according to (15), the pressure is

$$p'(x, t) = \omega \rho^f a \sin(\phi(X_1 - X_0)) \sin(\omega t), \quad (24)$$

or

$$p(x, t) = p^0(t) + x \omega \rho^f a \sin(\phi(X_1 - X_0)) \sin(\omega t). \quad (25)$$

Matching the normal stresses at the interface (20) gives

$$\begin{aligned} p^0(t) + (X_1 + d(X_1, t)) \omega \rho^f a \sin(\phi(X_1 - X_0)) \sin(\omega t) \\ = -\frac{a \phi (2\mu^s + \lambda^s)}{\omega} \cos(\phi(X_1 - X_0)) \sin(\omega t), \end{aligned} \quad (26)$$

and this equations determines $p^0(t)$:

$$\begin{aligned} p^0(t) = - (X_1 + d(X_1, t)) \omega \rho^f a \sin(\phi(X_1 - X_0)) \sin(\omega t) \\ - \frac{a \phi (2\mu^s + \lambda^s)}{\omega} \cos(\phi(X_1 - X_0)) \sin(\omega t). \end{aligned} \quad (27)$$

TABLE 1. A group of parameters for the compressed parallel plates

ρ^f	ρ^s	μ^f	μ^s	λ^s	X_0	X_1	X_2	ϕ	a
1	2	2	10	100	3	4	5	1.75π	2

Let the initial displacement and velocity be $d(X, 0) = 0$ and $u(x, 0) = a \sin(\phi(X_1 - X_0))$ respectively. Since the fluid velocity, across the whole fluid domain, is the same as the velocity at the interface, by an integration in time, we know that the displacements of the fluid particles $\xi(X, t) = d(X_1, t)$ are independent of X as well. Therefore, $x - x_1(t) = X - X_1$. Based on this relation, the solutions for the FSI equations (15) to (21) are summarised as follows:

$$d(X, t) = \frac{a}{\omega} \sin(\phi(X - X_0)) \sin(\omega t), X \in [X_0, X_1], \quad (28)$$

$$p(x(X, t), t) = \left[(X - X_1) \omega \rho^f a \sin(\phi(X_1 - X_0)) - \frac{a \phi(2\mu^s + \lambda^s)}{\omega} \cos(\phi(X_1 - X_0)) \right] \sin(\omega t), \quad (29)$$

$$u(x, t) = a \sin(\phi(X_1 - X_0)) \cos(\omega t), x \in [X_1, X_2]. \quad (30)$$

The motion of the interface is included in the solution $d(X, t)$, i.e.: $X_1 + d(X_1, t)$. The boundary pressure is also included in the solution as:

$$\begin{aligned} \bar{p}(t) &= p(x_2(t), t) \\ &= \left[(X_2 - X_1) \omega \rho^f a \sin(\phi(X_1 - X_0)) - \frac{a \phi(2\mu^s + \lambda^s)}{\omega} \cos(\phi(X_1 - X_0)) \right] \sin(\omega t), \end{aligned} \quad (31)$$

which is periodic in time with a frequency of ω .

3.2. Comparison with Numerical Simulation

In this section, we compare the analytical solutions derived in the previous section with the one-velocity FSI method described in Appendix A. The implementation is based on FreeFem++ [21], using the parameter set in Table 1 as an example, for which the maximal solid displacement is around $5\% = 0.05/(X_1 - X_0)$ of the width of the solid domain.

Remark 1. The physical model, Lamé's equation (3), assumes small displacements, whereas the analytical solutions (28), (29), and (30) remain valid under large solid deformations, provided that the vertical components of velocity and displacement remain negligible. Numerically, it is challenging to maintain negligible vertical components under large deformations due to the moving mesh.

We consider computation domain of a $\Omega_1 = (X_2 - X_0) \times H = 2 \times 4$ rectangle and apply a periodic boundary condition at the top and bottom boundaries. We start from a relative coarse mesh with 861 nodes and 1600 triangles as shown in Figure 3, and a time step of $\Delta t = 10^{-3}$ to compute up to a time of $T_1 = 0.5$ which is more than 3 time periods of oscillations. All the numerical results of velocity, pressure and displacement already agree well with our analytical solutions on this coarse mesh as shown in Figure 3, although we observe that the errors increase gradually as time evolves.

Based on the coarse mesh (Figure 3) and $\Delta t = 10^{-3}$, we refine the mesh and reduce the time step to test the spatiotemporal convergence of the numerical methods using $L^2([0, T_1]; L^2(\Omega_1))$ norm: first compute the $L^2(\Omega_1)$ error given a specific time, denoted by $e(t)$, then compute $L^2([0, T_1])$ norm of $e(t)$. We use a backward Euler scheme for the time discretisation and P_2P_1 element for the space discretisation of the velocity-pressure pair. The optimal spatiotemporal convergence is achieved as shown in Figure 4.

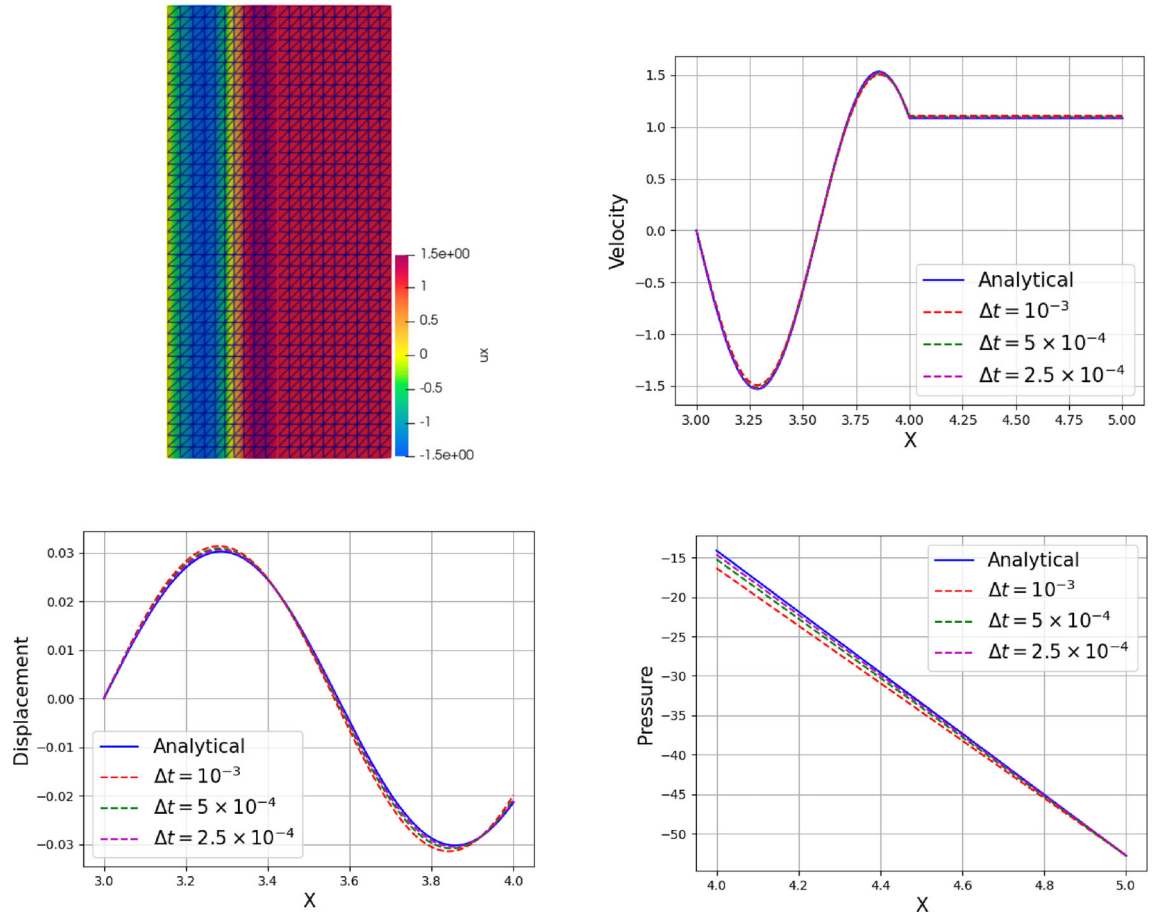


FIG. 3. Diagram showing the numerical result as well as its comparison with the analytical solutions at $t = 0.5$: from top to bottom, horizontal velocity on a coarse mesh, comparisons of the velocity, displacement and pressure

Remark 2. When $\phi(X_1 - X_0) = n\pi$ with $n \in \mathbb{N}$, $u(x, t) \equiv 0$. In this special case, the entire fluid remains stationary, while a compressed solid wave oscillates across $[X_0, X_1]$, with the boundary pressure $\bar{p}(t)$ passing through the fluid and directly acting on the solid. A brief discussion of this case is provided in Appendix B.1, along with supporting animations available at: <https://yongxingwang.github.io/analyticalfsi/>.

A similar observation can be found in [19], which presents explicit solutions for a generalised Taylor–Couette system.

4. Problem II: Compressed Concentric Discs

In this problem, both the fluid velocity and the solid displacement only have components along the radial direction: $\mathbf{u} = u\mathbf{e}_r$ and $\mathbf{d} = d\hat{\mathbf{e}}_r$. Additionally, both $u = u(r, t)$ and $d = d(R, t) = r - R$ are independent of $\theta = \hat{\theta}$, and the pressure $p = p(r, t)$ is also independent of θ (or $\hat{\theta}$). Let $u' = \partial_r u$ and $p' = \partial_r p$ for notation convenience.

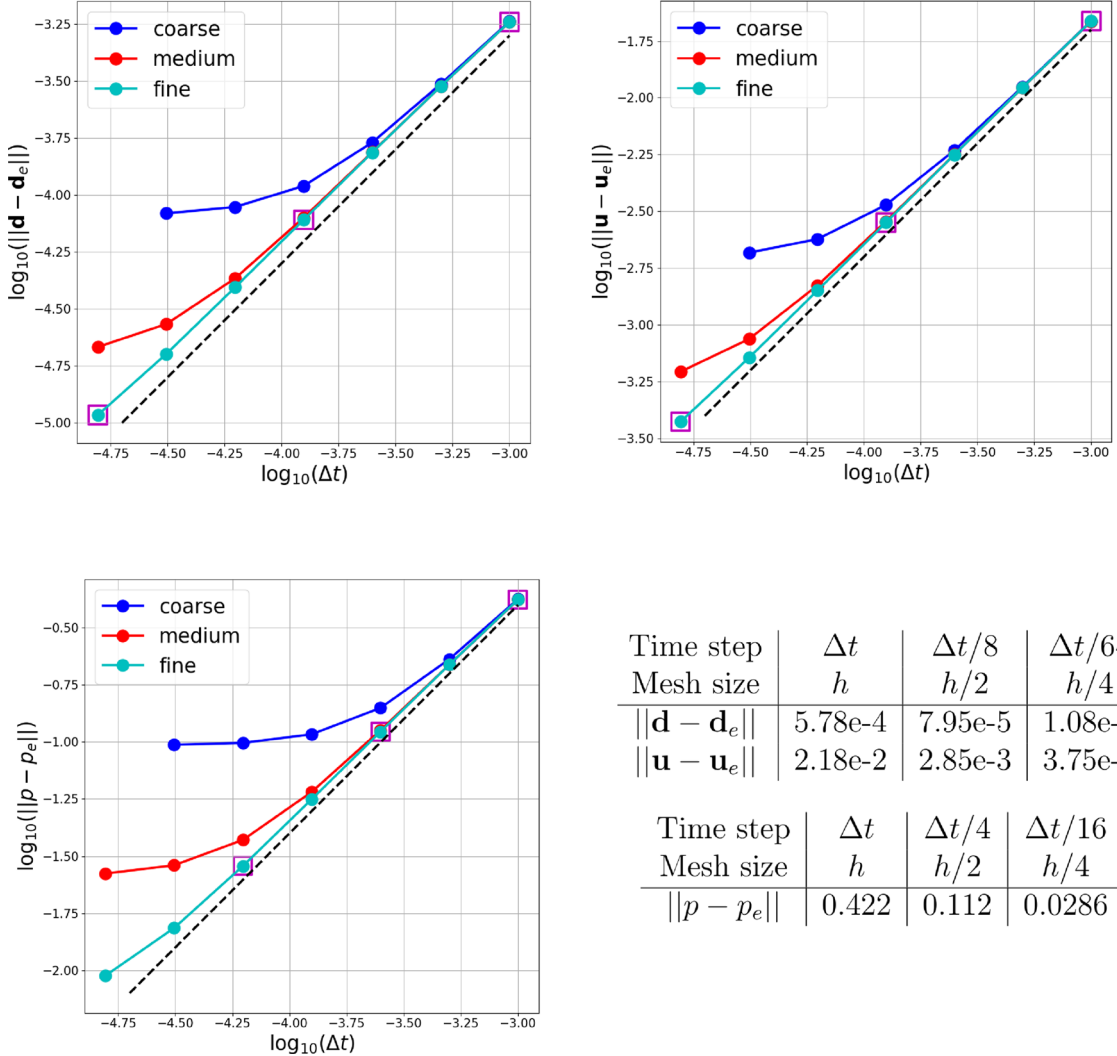


FIG. 4. Spatiotemporal convergence of the displacement, velocity and pressure in space $L^2([0, T_1]; L^2(\Omega_1))$, where Ω_1 is the reference computational domain at $t = 0$. The two tables show the errors corresponding to the squared points in the graphs, which indicate the optimal convergence of backward Euler and P_2P_1 element for the time and the space discretisations respectively. The size of the coarse mesh is $h = 0.1$ and the initial time step is $\Delta t = 10^{-3}$

4.1. Fluid Equations

Noticing that $\dot{\mathbf{e}}_r = \dot{\theta}\mathbf{e}_\theta = (u_\theta/r)\mathbf{e}_\theta = 0$, the inertial term can be expressed as:

$$\dot{\mathbf{u}} = \frac{d}{dt}(u_r \mathbf{e}_r) = \dot{u} \mathbf{e}_r = (\partial_t u + uu') \mathbf{e}_r. \quad (32)$$

Applying operator $\nabla \cdot \nabla$ to $\mathbf{u} = u_r \mathbf{e}_r$, we have

$$\nabla \cdot \nabla \mathbf{u} = \left(u'' + \frac{u'}{r} - \frac{u}{r^2} \right) \mathbf{e}_r. \quad (33)$$

These then yield the momentum equation

$$\rho^f(\partial_t u + uu') = \mu^f \left(u'' + \frac{u'}{r} - \frac{u}{r^2} \right) - p', \quad (34)$$

by substituting equations (32) and (33) into (1).

The continuity equation (2) becomes:

$$\nabla \cdot \mathbf{u} = \left(\mathbf{e}_r \partial_r + \frac{1}{r} \mathbf{e}_\theta \partial_\theta \right) \cdot (u \mathbf{e}_r) = u' + \frac{u}{r} = \frac{(ru)'}{r} = 0. \quad (35)$$

Finally, equation (35) may be substituted into equation (34) to obtain a simplified form of the momentum equation:

$$\rho^f(\partial_t u + uu') + p' = \mu^f(u' + \frac{u}{r})' = 0. \quad (36)$$

4.2. Solid Equations

Apply the operators $\hat{\nabla}$ and $\hat{\nabla} \cdot \hat{\nabla}$ to the displacement vector, and let $d' = \partial_R d$, then

$$\hat{\nabla} \mathbf{d} = \left(\hat{\mathbf{e}}_r \partial_R + \frac{1}{R} \hat{\mathbf{e}}_\theta \partial_\theta \right) (d \hat{\mathbf{e}}_r) = d' \hat{\mathbf{e}}_r \hat{\mathbf{e}}_r + \frac{d}{R} \hat{\mathbf{e}}_\theta \hat{\mathbf{e}}_\theta, \quad (37)$$

$$\hat{\nabla}^\top \mathbf{d} = d' \hat{\mathbf{e}}_r \hat{\mathbf{e}}_r + \frac{d}{R} \hat{\mathbf{e}}_\theta \hat{\mathbf{e}}_\theta = \hat{\nabla} \mathbf{d}, \quad (38)$$

$$\hat{\nabla} \cdot \hat{\nabla} \mathbf{d} = \left(d'' + \frac{d'}{R} - \frac{d}{R^2} \right) \hat{\mathbf{e}}_r. \quad (39)$$

Similar to the continuity equation of the fluid,

$$\hat{\nabla} \cdot \mathbf{d} = \left(\hat{\mathbf{e}}_r \partial_R + \frac{1}{R} \hat{\mathbf{e}}_\theta \partial_\theta \right) \cdot (d \hat{\mathbf{e}}_r) = d' + \frac{d}{R}, \quad (40)$$

which however is not zero. Instead, applying the gradient operator (12) to $\hat{\nabla} \cdot \mathbf{d}$, we have

$$\begin{aligned} \hat{\nabla}(\hat{\nabla} \cdot \mathbf{d}) &= \left(\hat{\mathbf{e}}_r \partial_R + \frac{1}{R} \hat{\mathbf{e}}_\theta \partial_\theta \right) \left(d' + \frac{d}{R} \right) \\ &= \left(d' + \frac{d}{R} \right)' \hat{\mathbf{e}}_r. \end{aligned} \quad (41)$$

Finally, substituting equations (39) and (41) into the solid equation (3), we obtain

$$\rho^s \ddot{d} = (2\mu^s + \lambda^s) \left(d' + \frac{d}{R} \right)'. \quad (42)$$

4.3. Boundary Conditions

As discussed in Section 3, the fluid equation (36) is expressed in the current or physical domain corresponding to the reference domain $[R_1, R_2]$, while the solid equation (42) is expressed directly in the reference domain $[R_0, R_1]$. We use again the Lagrangian mapping to find the current domain for the fluid, i.e., extending the solid displacement $d(R, t)$ ($R \in [R_0, R_1]$) to the displacement of the fluid particles $\xi(R, t)$ ($R \in [R_1, R_2]$), with $\xi(R_1, t) = d(R_1, t)$ at the interface. Let $r_1(t) = R_1 + \xi(R_1, t)$ and $r_2(t) = R_2 + \xi(R_2, t)$, then $r(R, t) = R + \xi(R, t)$ with $R \in [R_1, R_2]$ represents a general point in the current domain $[r_1(t), r_2(t)]$.

With the above notations, the continuity of normal stress at $R = R_1$ or $r = r_1(t)$ requires that:

$$\begin{aligned} & \mu^s (\hat{\nabla} \mathbf{d} + \hat{\nabla}^\top \mathbf{d}) \cdot \hat{\mathbf{e}}_r + \lambda^s (\hat{\nabla} \cdot \mathbf{d}) \mathbf{I} \cdot \hat{\mathbf{e}}_r \\ &= \mu^f (\nabla \mathbf{u} + \nabla^\top \mathbf{u}) \cdot \mathbf{e}_r - p \mathbf{I} \cdot \mathbf{e}_r \end{aligned} \quad (43)$$

or equivalently,

$$\begin{aligned} & 2\mu^s \left(d'(R_1, t) \hat{\mathbf{e}}_r \hat{\mathbf{e}}_r + \frac{d(R_1, t)}{R_1} \hat{\mathbf{e}}_\theta \hat{\mathbf{e}}_\theta \right) \cdot \hat{\mathbf{e}}_r \\ &+ \lambda^s \left(d'(R_1, t) + \frac{d(R_1, t)}{R_1} \right) (\hat{\mathbf{e}}_r \hat{\mathbf{e}}_r + \hat{\mathbf{e}}_\theta \hat{\mathbf{e}}_\theta) \cdot \hat{\mathbf{e}}_r \\ &= \mu^f \left(u'(r_1, t) \mathbf{e}_r \mathbf{e}_r + \frac{u(r_1, t)}{r_1(t)} \mathbf{e}_\theta \mathbf{e}_\theta \right) \cdot \mathbf{e}_r - \\ & p(r_1, t) (\mathbf{e}_r \mathbf{e}_r + \mathbf{e}_\theta \mathbf{e}_\theta) \cdot \mathbf{e}_r. \end{aligned} \quad (44)$$

\Rightarrow

$$\begin{aligned} & 2\mu^s d'(R_1, t) + \lambda^s \left(d'(R_1, t) + \frac{d(R_1, t)}{R_1} \right) \\ &= \mu^f u'(r_1, t) - p(r_1, t). \end{aligned} \quad (45)$$

Other boundary conditions include:

$$d(R_0, t) = 0 \quad (46)$$

$$\dot{d}(R_1, t) = u(r_1(t), t) \quad (47)$$

$$\mu^f u'(r_2, t) - p(r_2, t) = \bar{p}(t) \quad (48)$$

where (48) specifies the normal stress at the outer fluid boundary.

4.4. Analytical Solution

Assuming the solution of equation (42) is periodic and separable with respect to R and t , then it can be represented by the real or imaginary part of a complex form: $d(R, t) = z(R)e^{i\omega t}$. This representation enables us to derive the equation for $z(R)$ by substituting $z(R)e^{i\omega t}$ into (42), yielding:

$$-\rho^s \omega^2 z = (2\mu^s + \lambda^s) \left(z'' + \frac{z'}{R} - \frac{z}{R^2} \right). \quad (49)$$

Let $\sqrt{\rho^s \omega^2 / (2\mu^s + \lambda^s)} = k^s$, the above equation can be rewritten as:

$$R^2 z'' + R z' + [(k^s R)^2 - 1] z = 0. \quad (50)$$

By change of variable: $k^s R = x$, the above equation becomes the Bessel's ODE of order one.

$$x^2 \frac{d^2 z}{dx^2} + x \frac{dz}{dx} + (x^2 - 1) z = 0, \quad (51)$$

with a general solution

$$z(R(x)) = c_1 J_1(x) + c_2 Y_1(x), \quad (52)$$

where $J_1(x)$ and $Y_1(x)$ are the first and second kind Bessel functions, respectively, of order one as follows:

$$J_1(x) = \sum_{m=0}^{\infty} \frac{(-1)^m}{m!(m+1)!} \left(\frac{x}{2} \right)^{2m+1}, \quad (53)$$

$$\begin{aligned} \frac{\pi}{2} Y_1(x) &= \left(\gamma + \ln \frac{x}{2} \right) J_1(x) - \frac{1}{x} \\ &\quad + \frac{1}{2} \sum_{m=1}^{\infty} \frac{(-1)^m (H_{m-1} + H_m)}{(m-1)! m!} \left(\frac{x}{2} \right)^{2m-1}, \end{aligned} \quad (54)$$

with $H_0 = 0$, $H_m = 1 + 1/2 + 1/3 + \dots + 1/m$ and $\gamma = \lim_{m \rightarrow \infty} (H_m - \ln m)$. The solution of equation (50) can then be expressed as:

$$z(R) = c_1 J_1(k^s R) + c_2 Y_1(k^s R), \quad (55)$$

with the constants c_1 and c_2 being determined by the boundary conditions later. Let the $d(R, t) = z(R) \sin(\omega t)$ being the solution of (42), we derive the solution of fluid equations (35) and (36) as follows:

First, the continuity equation (35) indicates that ru is a constant: independent of r but possibly dependent of t . Recall the mapping between $r \in [r_1(t), r_2(t)]$ and $R \in [R_1, R_2]$: $r(R, t) = R + \xi(R, t)$, we have

$$ru = (R_1 + d(R_1, t)) \dot{d}(R_1, t), \quad (56)$$

due to the interface condition (47). This solves for the fluid velocity as:

$$u(r, t) = \frac{[R_1 + z(R_1) \sin(\omega t)] z(R_1) \omega \cos(\omega t)}{r}. \quad (57)$$

Notice that the initial condition of the velocity is determined by the expression in (57), which cannot be zero generally, although the initial condition for the displacement is zero. The pressure can then be solved by the momentum equation (36)

$$\begin{aligned} p'(r, t) &= \frac{z(R_1) \rho^f \omega^2 [R_1 \sin(\omega t) - z(R_1) \cos(2\omega t)]}{r} \\ &\quad - \rho^f \frac{(u^2)'_r}{2}. \end{aligned} \quad (58)$$

Integrate to obtain the expression of $p(x, t)$:

$$\begin{aligned} p(r, t) &= z(R_1) \rho^f \omega^2 [R_1 \sin(\omega t) - z(R_1) \cos(2\omega t)] \ln |r| \\ &\quad - \rho^f \frac{u^2(r, t)}{2} + p^0(t). \end{aligned} \quad (59)$$

The constant p^0 can be computed using the continuity of normal stress at the interface, equation (45):

$$\begin{aligned} &(2\mu^s + \lambda^s) z'(R_1) \sin(\omega t) + \lambda^s z(R_1) \sin(\omega t) / R_1 \\ &= \mu^f u'(r_1, t) - p(r_1, t), \end{aligned} \quad (60)$$

\Rightarrow

$$\begin{aligned} -p^0(t) &= (2\mu^s + \lambda^s) z'(R_1) \sin(\omega t) + \lambda^s z(R_1) \sin(\omega t) / R_1 \\ &\quad + \frac{\mu^f z(R_1) \omega \cos(\omega t)}{r_1(t)} - \rho^f \frac{u^2(r_1(t), t)}{2} \\ &\quad + z(R_1) \rho^f \omega^2 [R_1 \sin(\omega t) - z(R_1) \cos(2\omega t)] \ln |r_1(t)|. \end{aligned} \quad (61)$$

Substituting (61) into (59), we have

$$\begin{aligned} p(r, t) &= z(R_1) \rho^f \omega^2 [R_1 \sin(\omega t) - z(R_1) \cos(2\omega t)] \ln \left| \frac{r}{r_1(t)} \right| \\ &\quad - \rho^f \frac{u^2(r, t) - u^2(r_1(t), t)}{2} - \frac{\mu^f z(R_1) \omega \cos(\omega t)}{r_1(t)} \\ &\quad - (2\mu^s + \lambda^s) z'(R_1) \sin(\omega t) - \lambda^s z(R_1) \sin(\omega t) / R_1, \end{aligned} \quad (62)$$

where $r_1(t) = R_1 + z(R_1) \sin(\omega t)$.

Finally, the two constants c_1 and c_2 in the expression of $z(R)$ can be determined by two boundary conditions: (46) $\Rightarrow z(R_0) = 0$ and (48) $\Rightarrow p(r_2, t) = \mu^f u'(r_2, t) - \bar{p}(t)$, given $\bar{p}(t)$. However, because of the

complicated form of $p(r, t)$ as expressed in (62), it is difficult to solve for $z(R_1)$ from the second condition. We simply specify $z(R_1)$ as \bar{d} – the largest displacement at R_1 , to determine the constants c_1 and c_2 first, and then write down the expression of $\bar{p}(t)$ for the problem. To express c_1 and c_2 explicitly, we have the linear system

$$z(R_0) = J_1(k^s R_0)c_1 + Y_1(k^s R_0)c_2 = 0, \quad (63)$$

$$z(R_1) = J_1(k^s R_1)c_1 + Y_1(k^s R_1)c_2 = \bar{d}, \quad (64)$$

whose solution can be written as:

$$\begin{pmatrix} c_1 \\ c_2 \end{pmatrix} = \frac{1}{\det} \begin{pmatrix} Y_1(k^s R_1) & -Y_1(k^s R_0) \\ -J_1(k^s R_1) & J_1(k^s R_0) \end{pmatrix} \begin{pmatrix} 0 \\ \bar{d} \end{pmatrix}, \quad (65)$$

where $\det = J_1(k^s R_0)Y_1(k^s R_1) - J_1(k^s R_1)Y_1(k^s R_0)$.

Our implementation of the Bessel functions is based on the `scipy.special` library [6].

4.5. Mapping Between r and R

Since the solutions of the fluid and solid components are expressed in different configurations, it is necessary to explicitly define the mapping between r and R in order to display and visualise results – such as plotting the velocity field across the entire domain $[R_0, R_2]$. For $R \in [R_0, R_1]$, the mapping is given by $r = R + z(R) \sin(\omega t)$. For $R \in [R_1, R_2]$, the mapping can be determined by solving equation (56).

$$\begin{aligned} ru &= \frac{d}{dt} \left(\frac{r^2(R, t)}{2} \right) = (R_1 + z(R_1) \sin(\omega t)) z(R_1) \omega \cos(\omega t) \\ &\Rightarrow \frac{r^2(R, t)}{2} = R_1 z(R_1) \sin(\omega t) + \int z^2(R_1) \frac{\omega \sin(2\omega t)}{2} dt \\ &\Rightarrow \frac{r^2(R, t)}{2} = R_1 z(R_1) \sin(\omega t) - z^2(R_1) \frac{\cos(2\omega t)}{4} + C(R). \end{aligned}$$

Since $r(R, 0) = R \Rightarrow C(R) = R^2/2 + z^2(R_1)/4$, therefore,

$$\begin{aligned} \frac{r^2(R, t)}{2} &= R_1 z(R_1) \sin(\omega t) + z^2(R_1) \frac{\sin^2(\omega t)}{2} + \frac{R^2}{2} \\ &\Rightarrow r^2(R, t) = R^2 + (R_1 + z(R_1) \sin(\omega t))^2 - R_1^2, \end{aligned}$$

which is the relation between r and R .

Remark 3. Equation (42) possesses another form of solution: $d(R, t) = z(R)t$, where $z(R) = C_1 R + R/C_2$ represents the steady-state solution for (42) – an Euler PDE, with C_1 and C_2 being two constants. Consequently, this would yield an alternative solution for the FSI problem, though with distinct boundary conditions.

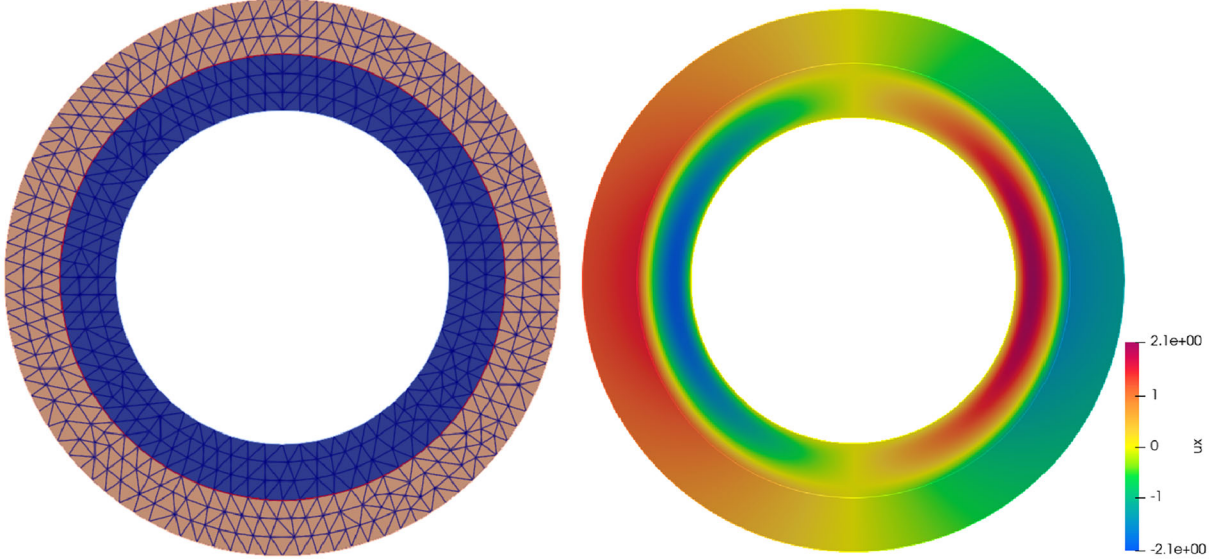
4.6. Comparison with Numerical Simulation

We compare the analytical solutions of the solid displacement $d(R, t) = z(R) \sin(\omega t)$ as well as its velocity $u(R, t) = z(R) \omega \cos(\omega t)$, together with the fluid velocity (57) and pressure (62), to the results of two-dimensional numerical simulations. We compare all the quantities in the reference configuration based on the mapping as described in Section 4.5: the results for a typical parameter set shown in Table 2. We set $z(R_1) = \bar{d} = 0.05$ to compute the coefficients c_1 and c_2 in (64), which is $\bar{d}/(R_1 - R_0) = 5\%$ of deformation of the width of the solid domain.

It can be seen in Figure 6 how the simulation results, based on a relatively coarse mesh (see Figure 5), converge to the analytical solution over time. The evolution of the fluid-solid interface is plotted in Figure 7, from which it can be observed that the error gradually increases as time progresses.

TABLE 2. A group of parameters for the compressed disc

ρ^f	ρ^s	μ^f	μ^s	λ^s	R_0	R_1	R_2	ω
1	2	2	10	100	3	4	5	2π

FIG. 5. A coarse mesh with 572 nodes and 1225 triangle (left), and the horizontal velocity profile at $t = 0.5$ (right)

The results of the spatiotemporal convergence are shown in Figure 8, with the bottom figure illustrating the temporal convergence of the $L^2(\Omega_2^f)$ and $L^2(\Omega_2^s)$ errors at $T_2 = 0.5$ on the medium mesh. Here, Ω_2^f and Ω_2^s denote the reference fluid and solid computational domains at $t = 0$, respectively. We find that the time convergence rate is not optimal; this is because there is an accumulated error when comparing the last figure (bottom-right) in Figure 8 to the other three. The accumulated error may be due to our implementation of the Bessel functions and the data transfer between Python and FreeFem++, which needs further investigations. The lack of optimal mesh convergence is understandable because FreeFem++ does not use isoparametric mesh for P_2P_1 elements. Our focus here is on validating the analytical solution, leaving the testing of the convergence rate of the numerical scheme for future study.

Remark 4. This problem can pose significant challenges for numerical simulations when moving the mesh, particularly when multiple compression waves propagate within the solid. For instance, setting $R_0 = 1$ in the parameter set outlined in Table 2 and $\bar{d} = 0.15$ (equivalent to 5% of the width of the solid domain $R_1 - R_0$) results in the emergence of a rapidly propagating wave within the solid, as illustrated in Figure 12.

5. Problem III: Rotating Concentric Discs

We assume pure rotation for this problem. For the fluid, the velocity vector $\mathbf{u} = u\mathbf{e}_\theta$ only has the tangential component $u = u(r, t)$, which is independent of θ . The pressure $p = p(r, t)$ is also independent of θ . For the solid, pure rotation means $r = R$ is independent of time in the position vector $r\mathbf{e}_r$, so its velocity, $\frac{d}{dt}(r\mathbf{e}_r) = r\dot{\theta}\mathbf{e}_\theta$, only has the tangential component. Assuming the angular displacement $\alpha = \theta - \hat{\theta} = \alpha(r, t)$ is independent of $\hat{\theta}$, then $\theta = \alpha + \hat{\theta}$, $\partial_r\theta = \partial_r\alpha$, and $\partial_\theta\theta = 1$, which will be used

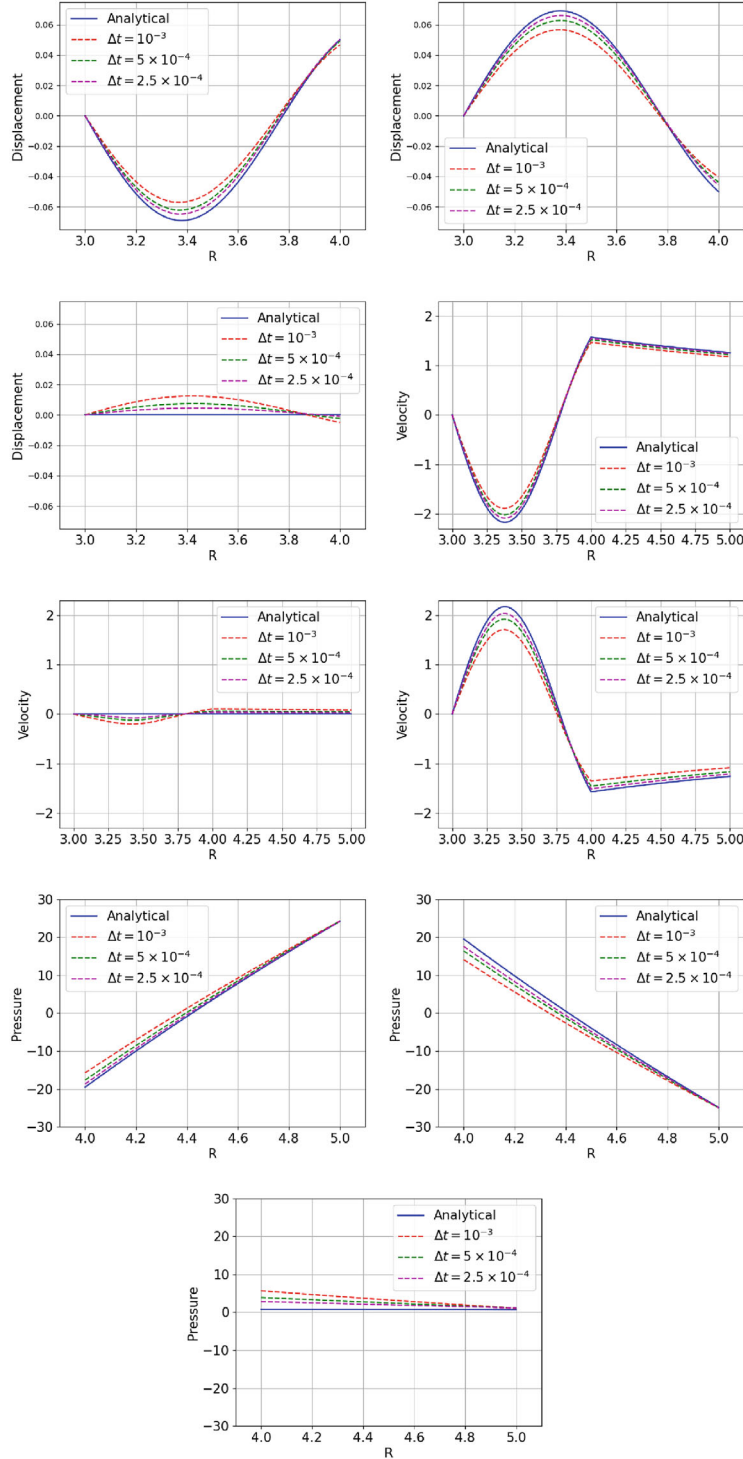


FIG. 6. Comparison of displacement (first row), velocity (second row), pressure (third row) at $t = 0.25$, $t = 0.35$ and $t = 0.5$ from left to right, except the plot of velocity at the second row and first column which is at $t = 0.2$, because the velocity profile at $t = 0.25$ is very similar to $t = 0.35$

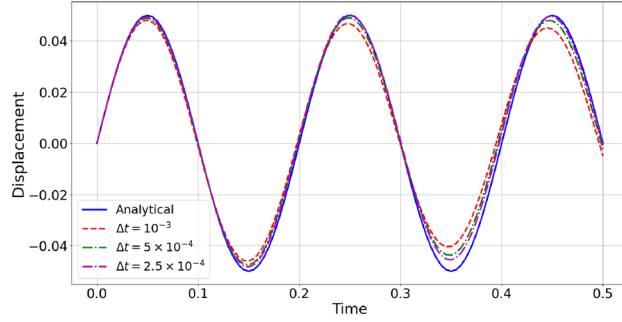


FIG. 7. Displacement of the interface as a function of time

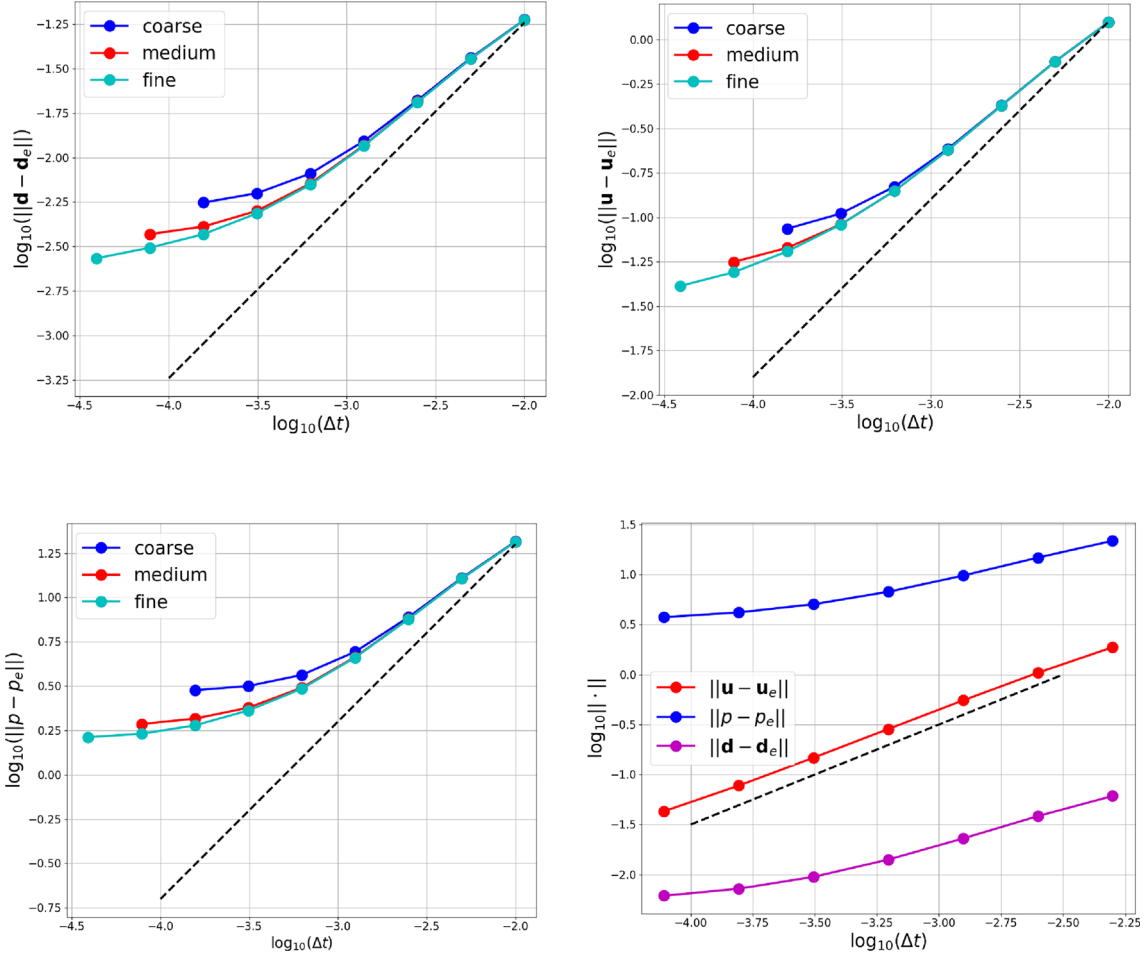


FIG. 8. From top to bottom, the first three plots display the spatiotemporal convergence of displacement, velocity, and pressure in the space $L^2([0, T_2]; L^2(\Omega_2))$, where $T_2 = 0.5$, and Ω_2 denotes the reference computational domain at $t = 0$. Specifically, Ω_2 corresponds to Ω_2^f (the fluid domain) when evaluating the errors in \mathbf{u} and p , and to Ω_2^s (the solid domain) when computing the error in \mathbf{d} . The final plot shows the temporal convergence of the $L^2(\Omega_2)$ errors in velocity, displacement, and pressure at $T_2 = 0.5$, computed on the medium mesh. The mesh size is defined by the maximum element diameter

in the following derivations. Finally, let $\dot{u} = \frac{du}{dt}$, $\dot{\alpha} = \frac{d\alpha}{dt}$, $u' = \partial_r u$, and $\alpha' = \partial_r \alpha$ for the convenience of notation.

5.1. Fluid Equations

Since $\dot{\mathbf{e}}_\theta = -\dot{\theta}\mathbf{e}_r = -(u/r)\mathbf{e}_r$, the inertial term can be expressed as:

$$\dot{\mathbf{u}} = \dot{u}\mathbf{e}_\theta - (u^2/r)\mathbf{e}_r. \quad (66)$$

Apply the gradient operator to $\mathbf{u} = u\mathbf{e}_\theta$, we have

$$\begin{aligned} \nabla \mathbf{u} &= \left(\mathbf{e}_r \partial_r + \mathbf{e}_\theta \frac{1}{r} \partial_\theta \right) (u\mathbf{e}_\theta) \\ &= \partial_r u \mathbf{e}_r \mathbf{e}_\theta - \frac{1}{r} u \mathbf{e}_\theta \mathbf{e}_r, \end{aligned} \quad (67)$$

and further:

$$\begin{aligned} \nabla \cdot \nabla \mathbf{u} &= \left(\partial_{rr} + \frac{1}{r} \partial_r + \frac{1}{r^2} \partial_{\theta\theta} \right) (u\mathbf{e}_\theta) \\ &= \left(\partial_{rr} u + \frac{1}{r} \partial_r u_\theta - \frac{u}{r^2} \right) \mathbf{e}_\theta. \end{aligned} \quad (68)$$

We also obtain:

$$\nabla p^f = \left(\mathbf{e}_r \partial_r + \mathbf{e}_\theta \frac{1}{r} \partial_\theta \right) p = \partial_r p^f \mathbf{e}_r. \quad (69)$$

The continuity equation (2) is automatically satisfied since

$$\nabla \cdot \mathbf{u} = \left(\mathbf{e}_r \partial_r + \frac{1}{r} \mathbf{e}_\theta \partial_\theta \right) \cdot (u\mathbf{e}_\theta) = 0. \quad (70)$$

Combining the above equations (66), (68) and (69), the momentum equation (1) can be expressed, in the polar coordinate system, as:

$$\rho^f \dot{u} = \mu^f (u'' + u'/r - u/r^2), \quad (71)$$

and

$$-\rho^f u^2/r = -\partial_r p^f. \quad (72)$$

5.2. Solid Equations

A large displacement formulation of an incompressible Neo-Hookean solid model is used in this paper. We apply the gradient operator $\hat{\nabla}$ to the position vector $r\mathbf{e}_r$ to compute the deformation tensor:

$$\begin{aligned} \mathbf{F} &= \hat{\nabla}(r\mathbf{e}_r) = \left(\hat{\mathbf{e}}_r \partial_R + \frac{1}{R} \hat{\mathbf{e}}_\theta \partial_{\hat{\theta}} \right) (r\mathbf{e}_r) \\ &= \hat{\mathbf{e}}_r \mathbf{e}_r + \hat{\mathbf{e}}_r \mathbf{e}_\theta (r\theta') + \hat{\mathbf{e}}_\theta \mathbf{e}_\theta, \end{aligned} \quad (73)$$

due to $\partial_R \mathbf{e}_r = \mathbf{e}_\theta \partial_R \theta = \mathbf{e}_\theta \theta'$ and $\partial_{\hat{\theta}} \mathbf{e}_r = \mathbf{e}_\theta \partial_{\hat{\theta}} \theta = \mathbf{e}_\theta$. Then,

$$\begin{aligned} \mathbf{F} \mathbf{F}^\top &= (\hat{\mathbf{e}}_r \mathbf{e}_r + \hat{\mathbf{e}}_r \mathbf{e}_\theta (r\theta') + \hat{\mathbf{e}}_\theta \mathbf{e}_\theta) \cdot (\mathbf{e}_r \hat{\mathbf{e}}_r + \mathbf{e}_\theta \hat{\mathbf{e}}_r (r\theta') + \mathbf{e}_\theta \hat{\mathbf{e}}_\theta) \\ &= [1 + (r\theta')^2] \hat{\mathbf{e}}_r \hat{\mathbf{e}}_r + (r\theta') \hat{\mathbf{e}}_r \hat{\mathbf{e}}_\theta + (r\theta') \hat{\mathbf{e}}_\theta \hat{\mathbf{e}}_r + \hat{\mathbf{e}}_\theta \hat{\mathbf{e}}_\theta, \end{aligned} \quad (74)$$

and further

$$\mathbf{F} \mathbf{F}^\top - \mathbf{I} = (r\theta')^2 \hat{\mathbf{e}}_r \hat{\mathbf{e}}_r + (r\theta') \hat{\mathbf{e}}_r \hat{\mathbf{e}}_\theta + (r\theta') \hat{\mathbf{e}}_\theta \hat{\mathbf{e}}_r. \quad (75)$$

In the spirit of expressing the solid equation in the current configuration, we replace $(\hat{\mathbf{e}}_r, \hat{\mathbf{e}}_\theta)$ by $(\mathbf{e}_r, \mathbf{e}_\theta)$ in equation (75) using the relation (13):

$$\mathbf{F}\mathbf{F}^\top - \mathbf{I} = \tau_{11}\mathbf{e}_r\mathbf{e}_r + \tau_{22}\mathbf{e}_\theta\mathbf{e}_\theta + \tau_{12}\mathbf{e}_\theta\mathbf{e}_r + \tau_{21}\mathbf{e}_r\mathbf{e}_\theta, \quad (76)$$

with $\tau_{11} = (r\alpha')^2 \cos^2 \alpha + (r\alpha') \sin(2\alpha)$, $\tau_{22} = (r\alpha')^2 \sin^2 \alpha - (r\alpha') \sin(2\alpha)$ and $\tau_{12} = \tau_{21} = (r\alpha') \cos(2\alpha) - \frac{(r\alpha')^2}{2} \sin(2\alpha)$, noticing that $\theta' = \alpha'$. We then have

$$\nabla \cdot (\mathbf{F}\mathbf{F}^\top - \mathbf{I}) = \partial_r \tau_{12}\mathbf{e}_\theta + \frac{2\tau_{12}}{r}\mathbf{e}_\theta + \partial_r \tau_{11}\mathbf{e}_r + \frac{\tau_{11} - \tau_{22}}{r}\mathbf{e}_r. \quad (77)$$

The inertial term is

$$\ddot{\mathbf{d}} = \frac{d^2}{dt^2}(r\mathbf{e}_r) = \frac{d}{dt}(r\dot{\alpha}\mathbf{e}_\theta) = r\ddot{\alpha}\mathbf{e}_\theta - r\dot{\alpha}^2\mathbf{e}_r, \quad (78)$$

bearing in mind that $\dot{\theta} = \dot{\alpha}$.

Substituting equations (77) and (78) into the solid equation (4), we have

$$\rho^s r \ddot{\alpha} = \mu^s [\partial_r \tau_{12} + 2\tau_{12}/r], \quad (79)$$

and

$$-\rho^s r \dot{\alpha}^2 = \mu^s [\partial_r \tau_{11} + (\tau_{11} - \tau_{22})/r] - \partial_r p^s. \quad (80)$$

5.3. Boundary and Initial Conditions

The continuity of normal stress at the interface $r = R_1$ indicates that:

$$\begin{aligned} \mu^s (\mathbf{F}\mathbf{F}^\top - \mathbf{I}) \cdot \mathbf{e}_r - p^s \mathbf{I} \cdot \mathbf{e}_r \\ = \mu^f (\nabla^\top \mathbf{u} + \nabla \mathbf{u}) \cdot \mathbf{e}_r - p^f \mathbf{I} \cdot \mathbf{e}_r, \end{aligned} \quad (81)$$

or

$$\mu^s (\tau_{11}\mathbf{e}_r + \tau_{12}\mathbf{e}_\theta) - p^s \mathbf{e}_r = \mu^f \left(u' - \frac{u}{r} \right) \mathbf{e}_\theta - p^f \mathbf{e}_r, \quad (82)$$

at $r = R_1$. Rewriting the boundary condition (82) in the directions of \mathbf{e}_θ and \mathbf{e}_r respectively yields:

$$\mu^s \tau_{12}(\alpha(R_1, t)) = \mu^f [u'(R_1, t) - u(R_1, t)/R_1], \quad (83)$$

$$\mu^s \tau_{11}(\alpha(R_1, t)) = p^s(R_1, t) - p^f(R_1, t). \quad (84)$$

Other boundary conditions include:

$$\alpha(R_0, t) = 0, \quad (85)$$

$$R_1 \dot{\alpha}(R_1, t) = u(R_1, t), \quad (86)$$

$$u(R_2, t) = \bar{u}(t). \quad (87)$$

Initial conditions are:

$$\alpha(r, 0) = \alpha_0 \quad \text{in } [R_0, R_1], \quad (88)$$

$$u(r, 0) = u_0 \quad \text{in } [R_1, R_2]. \quad (89)$$

5.4. A One-Velocity Monolithic Method

In this section, we use a finite element method to solve the velocity equation (71) of the fluid and the angular displacement equation (79) of the solid together in a fully-coupled manner. In addition, we express the angular displacement α in terms of velocity and only solve for one velocity field in domain $[R_0, R_2]$. For this method, the continuity of the velocity at the interface (86) is automatically satisfied. The pressure equations (72) and (80) are decoupled from the momentum equations, and will be solved as a post-process.

Given a test function

$$v(r) \in H_0^1[R_0, R_2] = \{v : v \in H^1[R_0, R_2], v(R_0, t) = 0\},$$

the weak form of (79) can be expressed as:

$$\begin{aligned} \rho^s \int_{R_0}^{R_1} r \ddot{\alpha} v dr &= \mu^s \tau_{12}(\alpha(R_1, t)) v(R_1) \\ &\quad + \mu^s \int_{R_0}^{R_1} \tau_{12}(\alpha) [2v/r - v'] dr. \end{aligned} \quad (90)$$

Considering the interface condition (83), the weak form of (71) may be expressed as:

$$\begin{aligned} \rho^f \int_{R_1}^{R_2} \dot{u} v dr \\ &= \mu^f \int_{R_1}^{R_2} [(u' - u/r)' + 2(u'/r - u/r^2)] v dr \\ &= -\mu^f [u'(R_1, t) - u(R_1, t)/R_1] dr \\ &\quad + \mu^f \int_{R_1}^{R_2} (u' - u/r)(2v/r - v') dr. \end{aligned} \quad (91)$$

The sum of equations (90) and (91) leads to the monolithic formulation as follows:

Given the initial values α_0 in (88) and u_0 in (89), find $u(r, t) \in H^1[R_0, R_2]$ such that $\forall v(r) \in H_0^1[R_0, R_2]$, the following equation holds:

$$\begin{aligned} \rho \int_{R_0}^{R_2} \dot{u} v dr &= \mu^s \int_{R_0}^{R_1} \tau_{12}(\alpha) [2v/r - v'] dr \\ &\quad + \mu^f \int_{R_1}^{R_2} (u' - u/r)(2v/r - v') dr, \end{aligned} \quad (92)$$

where $\rho = \rho^s 1_{[R_0, R_1]} + \rho^f 1_{[R_1, R_2]}$ and $r \dot{\alpha} = u$ in $[R_0, R_1]$.

Function $\tau_{12}(\alpha)$ in (92) is non-linear in terms of α , we use the Newton method to linearise it as follows:

$$\tau_{12}(\alpha) \approx \tau_{12}(\alpha^k) + \delta\tau_{12}(\alpha^k; \alpha - \alpha^k), \quad (93)$$

where α^k is a reference point and $\delta\tau_{12}(\alpha; \beta)$ is the first order Gateaux variation at α along direction β [5, 30]:

$$\delta\tau_{12}(\alpha; \beta) = \frac{d}{d\epsilon} \tau_{12}(\alpha + \epsilon\beta) \Big|_{\epsilon=0}. \quad (94)$$

With this definition, we compute the variations of $\tau_{12}(\alpha)$:

$$\begin{aligned} \delta\tau_{12}(\alpha; \delta\alpha) &= r\delta\alpha' \cos(2\alpha) - 2r\alpha' \sin(2\alpha)\delta\alpha \\ &\quad - r^2\alpha' \sin(2\alpha)\delta\alpha' - (r\alpha')^2 \cos(2\alpha)\delta\alpha, \end{aligned} \quad (95)$$

Substituting (95) into (93), with $\delta\alpha = \alpha - \alpha^k$, we have

$$\begin{aligned}\tau_{12}(\alpha) &\approx r\alpha' \cos(2\alpha^k) \\ &- 2r(\alpha^k)' \sin(2\alpha^k)(\alpha - \alpha^k) \\ &- r^2(\alpha^k)' \sin(2\alpha^k)(\alpha - \alpha^k)' \\ &- [r(\alpha^k)']^2 \cos(2\alpha^k)(\alpha - \alpha^k) \\ &- \frac{(r(\alpha^k)')^2}{2} \sin(2\alpha^k).\end{aligned}\tag{96}$$

Finally, we consider a descretisation in time. Given the previous values α_n and u_n at time t_n where $n = 0, 1, 2, \dots$, we use a uniform time step Δt to compute α_{n+1} and u_{n+1} . Since $r\dot{\alpha} = u$, we express $\alpha_{n+1} = \alpha_n + u_{n+1}\Delta t/r$ based on the backward Euler scheme. Dropping of the subscript $n+1$ for convenience, and substituting $\alpha = \alpha_n + u\Delta t/r$ and $\alpha' = \alpha'_n + \Delta t(u'/r - u/r^2)$, together with (96), to equation (92), we have the linearised one-velocity monolithic formulation after time discretisation:

Given α_n and u_n at time t_n , find $u_{n+1} = u(r, t) \in H^1[R_0, R_2]$ such that $\forall v(r) \in H_0^1[R_0, R_2]$, the following equation holds:

$$\begin{aligned}&\rho \int_{R_0}^{R_2} \frac{u - u_n}{\Delta t} v dr + \mu^f \int_{R_1}^{R_2} (u' - u/r)(v' - 2v/r) dr \\ &+ \mu^s \int_{R_0}^{R_1} \Delta t [\cos(2\alpha^k) - r(\alpha^k)' \sin(2\alpha^k)] (u' - u/r)(v' - 2v/r) dr \\ &- \mu^s \int_{R_0}^{R_1} \Delta t [r((\alpha^k)')^2 \cos(2\alpha^k) + 2(\alpha^k)' \sin(2\alpha^k)] u(v' - 2v/r) dr \\ &= \mu^s \int_{R_0}^{R_1} [-r\alpha'_n \cos(2\alpha^k) + 2r(\alpha^k)' \sin(2\alpha^k) (\alpha_n - \alpha^k)] \\ &(v' - 2v/r) dr \\ &+ \mu^s \int_{R_0}^{R_1} [r^2(\alpha^k)' \sin(2\alpha^k) (\alpha_n - \alpha^k)' + (r(\alpha^k)')^2 \\ &\cos(2\alpha^k) (\alpha_n - \alpha^k)] (v' - 2v/r) dr \\ &+ \mu^s \int_{R_0}^{R_1} \frac{(r(\alpha^k)')^2}{2} \sin(2\alpha^k) (v' - 2v/r) dr.\end{aligned}\tag{97}$$

The pressure is computed as a post-process. Integration of equation (80) from R_0 to $R \in (R_0, R_1]$ yields the expression of the pressure of solid:

$$\begin{aligned}p^s(R, t) &= \mu^s [\tau_{11}(\alpha(R)) - \tau_{11}(\alpha(R_0))] \\ &+ \mu^s \int_{R_0}^R \frac{\tau_{11} - \tau_{22}}{r} dr + \rho^s \int_{R_0}^R \frac{u^2}{r} dr,\end{aligned}\tag{98}$$

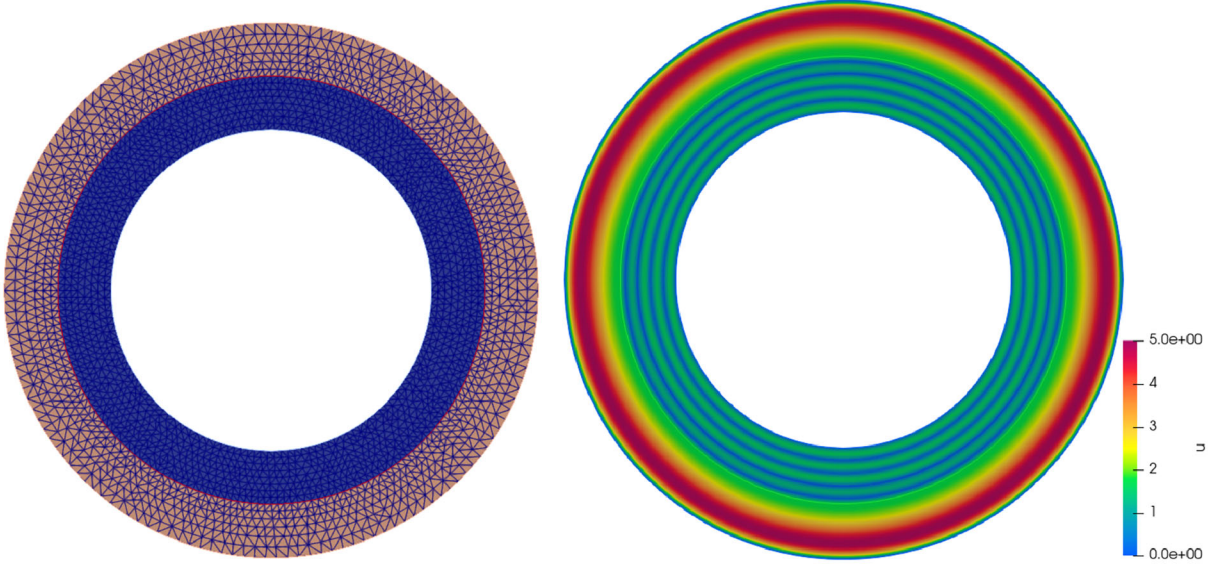
given a reference pressure $p^s(R_0, t) = 0$. Integration of equation (72) from R_1 to $R \in (R_1, R_2]$ yields the expression of the fluid pressure as follows:

$$p^f(R, t) = \rho^f \int_{R_1}^R \frac{u^2}{r} dr + p^f(R_1, t),\tag{99}$$

where $p^f(R_1, t) = p^s(R_1, t) - \mu^s \tau_{11}(\alpha(R_1))$ is known from the jump condition (84).

TABLE 3. A group of parameters for the rotating disc

ρ^f	ρ^s	μ^f	μ^s	R_0	R_1	R_2	ω
1	2	2	10	3	4	5	10π

FIG. 9. A coarse mesh with 2621 nodes and 5443 triangle and the magnitude of velocity profile at $t = 0.5$

5.5. Comparison with Numerical Simulation

It is efficient to solve the one-dimensional problem (97) to very high accuracy, a solution we refer to as the semi-analytical solution. We test a range of parameters and compare these semi-analytical solutions to those obtained from two-dimensional simulations using the numerical method described in A. We find that the one-dimensional and two-dimensional solutions agree very well. We report the results of the parameter set in Table 3, where a periodic angular velocity profile is prescribed at boundary R_2 : $\Omega(t) = \bar{\Omega} \sin(\omega t)$ with $\bar{\Omega} = 3$. Consequently, a complicated wave-like solution is created, and we have to use a relatively fine mesh to capture this feature. A finite element mesh and the magnitude of the velocity at $t = 1$ are displayed in Figure 9 to visualise the wave pattern.

The comparison of displacement, velocity, and pressure between the 1D and 2D simulations is depicted in Figure 10. It can be observed that the results for displacement and velocity show good agreement between the 1D and 2D simulations, while there is a noticeable discrepancy in pressure. We attribute this inconsistency in pressure to the discontinuity at $R = R_1$, despite employing the $P_2(P_1 + P_0)$ element [7], as can be seen in the last two plots of Figure 10. Consequently, there is a pressure shift within the fluid region, which in turn affects the accuracy of solid pressure as well.

6. Conclusion

In this paper, we propose three fluid-structure interaction problems and derive their analytical or semi-analytical solutions, which are compared with numerical experiments. These FSI solutions fill the gap in the analytical solutions within the FSI community and contribute to the field by benchmarking numerical methods for FSI problems.

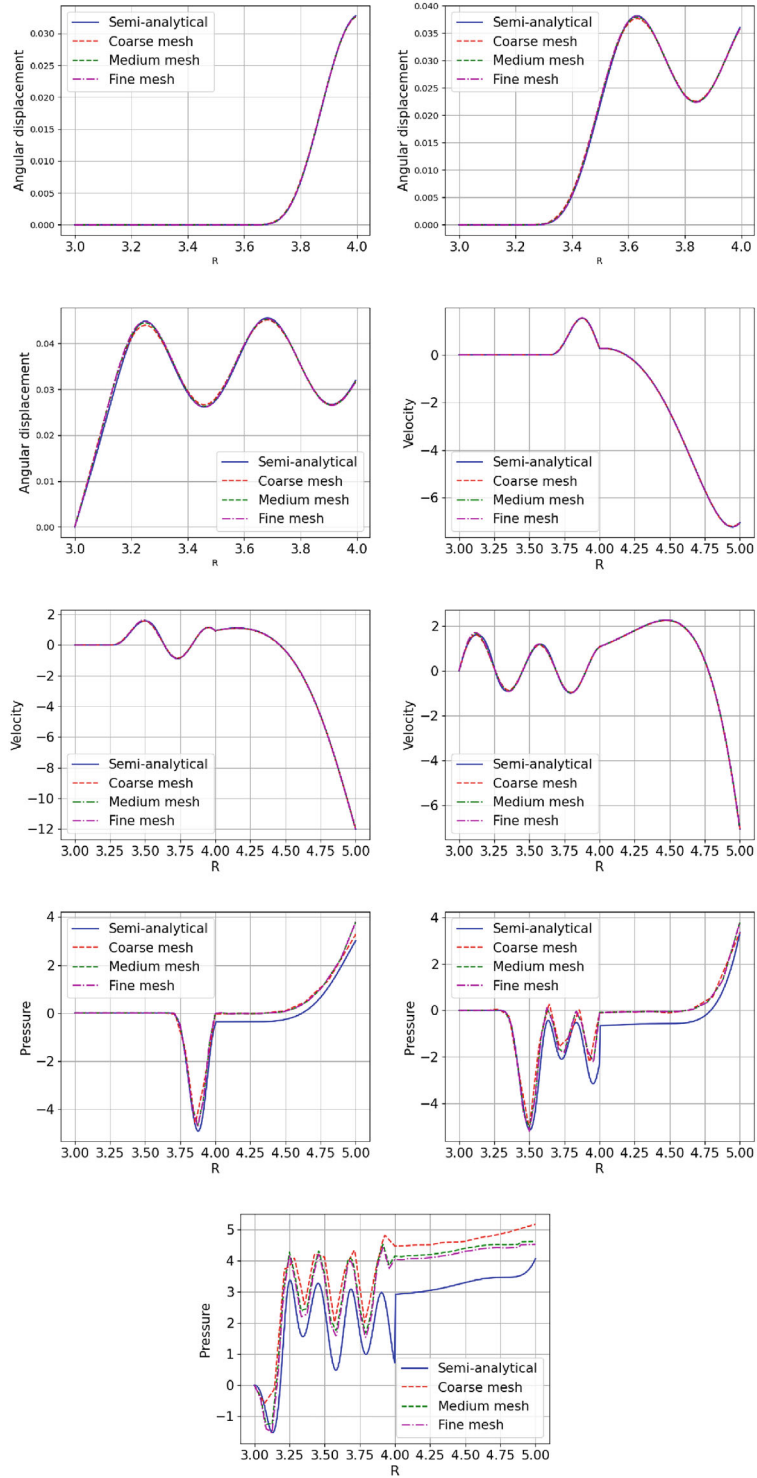


FIG. 10. Comparison of angular displacement (first row), velocity (second row), and pressure (third row) at $t = 0.2$, $t = 0.35$, and $t = 0.5$, from left to right. It is noteworthy that a maximum angular displacement of 0.045 corresponds to a maximum radial displacement of $0.045R_1 = 0.135$, which represents a 13.5% deformation of the width of the solid domain, $R_1 - R_0 = 1$

We also developed the one-velocity monolithic method to solve a one-dimensional non-linear problem (92) and a linear elastic problem in the reference domain (101). The one-velocity monolithic method is tested against the analytical solution, with results showing good agreement between them.

The results between the analytical and numerical solutions for the rotating disc (Problem III) do not align well for the pressure, although they match closely for the velocity and displacement. We attribute this discrepancy to the pressure discontinuity across the fluid-solid interface not being accurately captured in the numerical methods. Different numerical strategies, such as discontinuous finite elements or regularisation methods, may be explored in the future.

Data Availability Statement All the data and FreeFem code for the numerical tests are shared in the public GitHub repository: <https://github.com/yongxingwang>.

Declarations

Conflicts of interests On behalf of all authors, the corresponding author states that there is no conflict of interest.

Open Access. This article is licensed under a Creative Commons Attribution 4.0 International License, which permits use, sharing, adaptation, distribution and reproduction in any medium or format, as long as you give appropriate credit to the original author(s) and the source, provide a link to the Creative Commons licence, and indicate if changes were made. The images or other third party material in this article are included in the article's Creative Commons licence, unless indicated otherwise in a credit line to the material. If material is not included in the article's Creative Commons licence and your intended use is not permitted by statutory regulation or exceeds the permitted use, you will need to obtain permission directly from the copyright holder. To view a copy of this licence, visit <http://creativecommons.org/licenses/by/4.0/>.

Publisher's Note Springer Nature remains neutral with regard to jurisdictional claims in published maps and institutional affiliations.

A. The One-Velocity Numerical Methods for FSI Problems

In this section, we briefly introduce the numerical method used to simulate the two-dimensional FSI problems. We employ the monolithic Eulerian method, as discussed in several references [15, 22, 39], to solve for a single velocity variable across the entire FSI domain $\Omega_t^f \cup \Omega_t^s$.

Given the Cauchy stress tensor σ in the current configuration, the general weak form of this monolithic approach can be expressed as follows [39]:

$$\int_{\Omega} \rho \dot{\mathbf{u}} \delta \mathbf{u} + \int_{\Omega} \sigma : \nabla \delta \mathbf{u} = \int_{\partial \Omega} (\sigma \cdot \mathbf{n}) \cdot \delta \mathbf{u}, \quad (100)$$

where $\rho = \rho^f 1_{\Omega^f} + \rho^s 1_{\Omega^s}$, $\sigma = \sigma^f 1_{\Omega^f} + \sigma^s 1_{\Omega^s}$, and \mathbf{n} is the outer normal of domain Ω .

The one-velocity method aims to express the displacement $\mathbf{d}_{n+1} = \mathbf{d}_n + \Delta t \mathbf{u}_{n+1}$ after time discretisation, solving solely for the velocity \mathbf{u}_{n+1} at time t_{n+1} for the whole FSI problem, given \mathbf{u}_n and \mathbf{d}_n at time t_n . The primary objective is then to express $\int_{\Omega} \sigma : \nabla \delta \mathbf{u} = \int_{\Omega_t^f} \sigma^f : \nabla \delta \mathbf{u} + \int_{\Omega_t^s} \sigma^s : \nabla \delta \mathbf{u}$ in terms of displacement \mathbf{d} , which is discussed in the following.

The fluid integral expressions are the same for the three problems:

$$\begin{aligned} \int_{\Omega_t^f} \sigma^f : \nabla \delta \mathbf{u} &= \frac{\mu^f}{2} \int_{\Omega_t^f} (\nabla^T \mathbf{u} + \nabla \mathbf{u}) : (\nabla^T \delta \mathbf{u} + \nabla \delta \mathbf{u}) \\ &\quad - \int_{\Omega_t^f} p \nabla \cdot \delta \mathbf{u}, \end{aligned} \quad (101)$$

but they differ in the boundary integral expression concerning the Neumann boundary condition: $\sigma \cdot \mathbf{n} = \bar{p}(t) \mathbf{n}$ at boundary R_2 for Problem I and II, while $\sigma \cdot \mathbf{n} = 0$ for Problem III. They also vary in the solid stress tensor σ^s as described through the momentum equations (3) and (4).

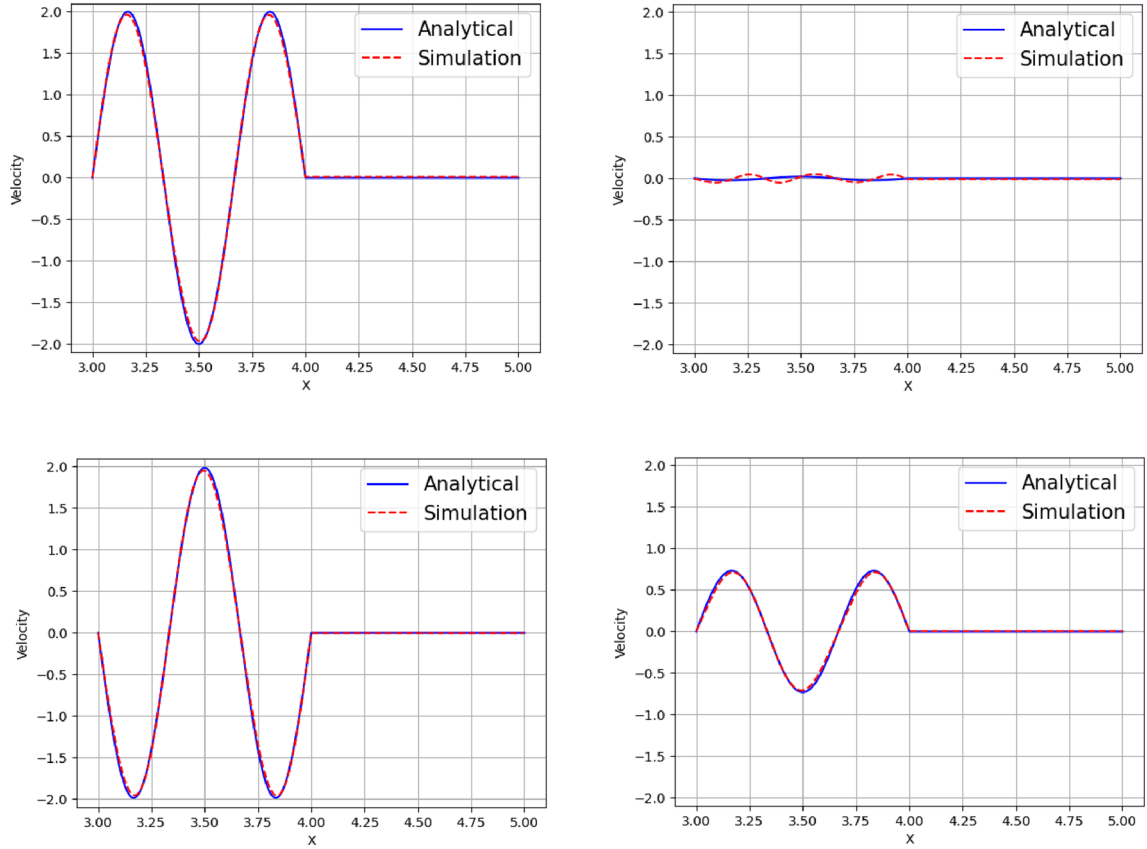


FIG. 11. Velocity profile at different times: $t = 0.43$, $t = 0.425$, $t = 0.475$ and $t = 0.5$ from left to right and top to bottom

For Problems I and II, the first Piola-Kirchhoff stress tensor $\mathbf{P} = \mu^s (\hat{\nabla}^\top \mathbf{d} + \hat{\nabla} \mathbf{d}) + \lambda^s (\hat{\nabla} \cdot \mathbf{d}) \mathbf{I}$ is used in the reference configuration, as seen in (3). To implement the monolithic Eulerian formulation, we convert \mathbf{P} to the Cauchy stress tensor and integrate as follows:

$$\begin{aligned} \int_{\Omega_t^s} \boldsymbol{\sigma}^s : \nabla \delta \mathbf{u} &= \int_{\Omega_t^s} J^{-1} \mathbf{P} \mathbf{F}^\top : \nabla \delta \mathbf{u} \\ &= \mu^s \int_{\Omega_t^s} J^{-1} (\mathbf{F}^\top \nabla^\top \mathbf{d} + \nabla \mathbf{d} \mathbf{F}) \mathbf{F}^\top : \nabla \delta \mathbf{u} \\ &\quad + \lambda^s \int_{\Omega_t^s} J^{-1} \text{trace}(\nabla \mathbf{d} \mathbf{F}) \text{trace}(\nabla \delta \mathbf{u} \mathbf{F}), \end{aligned} \quad (102)$$

where $\mathbf{F} = \hat{\nabla} \mathbf{d} + \mathbf{I} = \nabla \mathbf{d} \mathbf{F} + \mathbf{I} \Rightarrow \mathbf{F} = (\mathbf{I} - \nabla \mathbf{d})^{-1}$ is computed in the current configuration. As \mathbf{F} depends on the unknown variable, a fixed-point iteration is adopted to iteratively compute \mathbf{F} .

For Problem III, the Cauchy stress tensor $\boldsymbol{\sigma}^s = \mu^s (\mathbf{F} \mathbf{F}^\top - \mathbf{I}) - p^s \mathbf{I}$ is used as seen in (4), which can be rewritten as [39]:

$$\begin{aligned} \boldsymbol{\sigma}^s &= \mu^s (\nabla^\top \mathbf{d} + \nabla \mathbf{d} - \nabla^\top \mathbf{d} \nabla \mathbf{d}) \\ &\quad - (p^s + \mu^s (\text{trace}(\mathbf{F} \mathbf{F}^\top) - 2)) \mathbf{I}. \end{aligned} \quad (103)$$

For the numerical implementation of (103), we introduce a new variable $q^s = p^s + \mu^s (\text{trace}(\mathbf{F} \mathbf{F}^\top) - 2)$. Equation (103) is then expressed in terms of the displacement \mathbf{d} and the new pressure q^s .

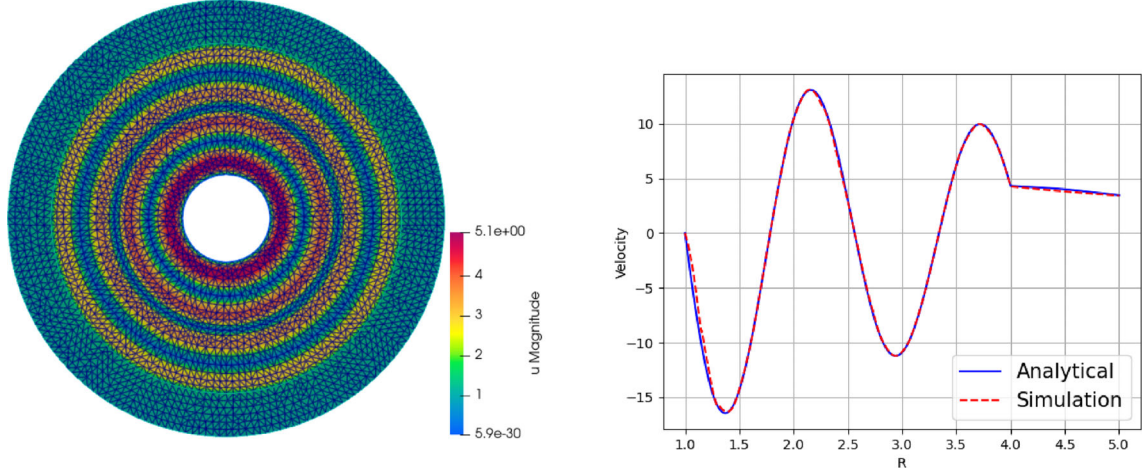


FIG. 12. Velocity magnitude on a 2D mesh (left) and velocity along the radial direction (right) at $t = 0.046$, when $R_0 = 1$ for numerical simulations with multiple compressed waves propagating in the solid. The simulation is run on a mesh of 3472 vertices and 7105 triangles with $\Delta t = 2.5 \times 10^{-4}$

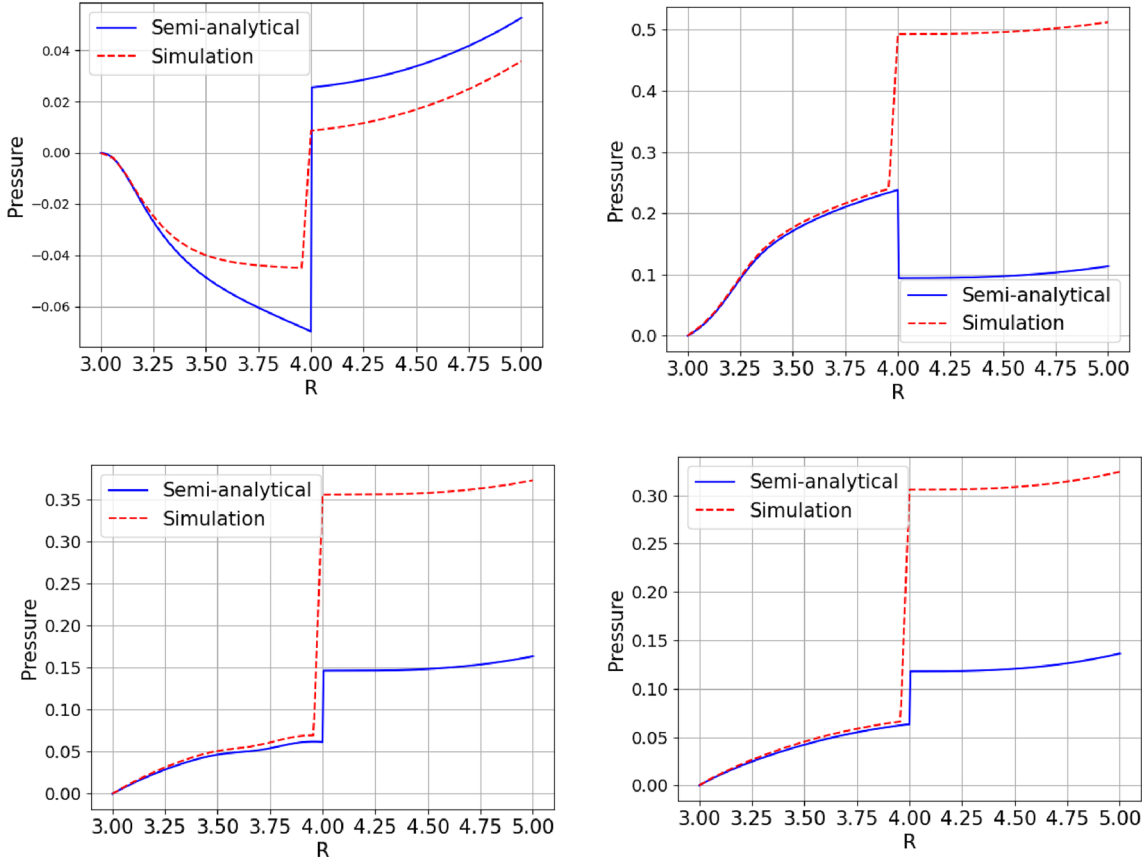


FIG. 13. Pressure of the rotating disc on a medium mesh with $\Delta t = 10^{-3}$ at different times: $t = 0.5$, $t = 1.5$, $t = 2$, and $t = 5$ from left to right and top to bottom. The steady-state solution is reached at $t = 5$

B. Additional Test Cases

In this appendix, we provide a brief report on the results of some additional, yet special, test cases as supplementary material to the main content of this article. Readers may also refer to additional supporting animations at:

<https://yongxingwang.github.io/analyticalfsi/>.

B.1. Problem I: Compressed Plates

Figure 11 shows the velocity profile, where the fluid velocity remains zero while there is a moving wave in the solid. This result is obtained by modifying the parameter set in Table 1 with $\phi = 3\pi$, in which case nothing happens in the fluid as commented in Remark 2.

B.2. Problem II: Compressed Discs

A challenging test case can be created simply by setting $R_0 = 1$ in the parameter set outlined in Table 2. As pointed out in Remark 4, a compressed wave propagates in the solid domain, causing the solid mesh to compress and stretch along the radial direction, as shown in Figure 12. We set $\bar{d} = 0.15$ (5% of the width of the solid domain $R_1 - R_0$) and tested a mesh of 3472 vertices and 7105 triangles, with a time step of 10^{-3} , alongside a remeshing technique to preserve mesh quality. Unfortunately, our simulation breaks down before reaching the maximum displacement at $t = 0.05$.

B.3. Problem III: Rotating Discs

To further explore the pressure, we test a simpler case than the one considered in Section 5.5: we use the same parameters as in Table 3, but prescribe a constant angular velocity $\Omega(t) = 0.1$ so that the rotating disc has a steady-state solution. We run the simulation up to $t = 5$ to ensure it reaches a steady-state solution. As shown in Figure 13, we again observe an inconsistency in the pressure between the 1D and 2D simulations. As the solution approaches the steady state, this inconsistency is only due to a constant shift of the fluid pressure, while the solid pressure agrees well.

References

- [1] Bai, W., Taylor, R.E.: Fully nonlinear simulation of wave interaction with fixed and floating flared structures. *Ocean Eng.* **36**(3), 223–236 (2009)
- [2] Basting, S., Quaini, A., Čanić, S., Glowinski, R.: Extended ALE method for fluid-structure interaction problems with large structural displacements. *J. Comput. Phys.* **331**, 312–336 (2017)
- [3] Bazilevs, Y., Hsu, M.C., Kiendl, J., Wüchner, R., Bletzinger, K.U.: 3D simulation of wind turbine rotors at full scale. Part II: fluid–structure interaction modeling with composite blades. *Int. J. Numer. Methods Fluids* **65**(1–3), 236–253 (2011)
- [4] Bazilevs, Y., Hsu, M.C., Zhang, Y., Wang, W., Kvamsdal, T., Hentschel, S., Isaksen, J.G.: Computational vascular fluid-structure interaction: methodology and application to cerebral aneurysms. *Biomech. Model. Mechanobiol.* **9**(4), 481–498 (2010). <https://doi.org/10.1007/s10237-010-0189-7>
- [5] Bazilevs, Y., Takizawa, K., Tezduyar, T.E.: Computational fluid-structure interaction: methods and applications. John Wiley & Sons (2013)
- [6] Blanco-Silva, F.J.: Learning SciPy for numerical and scientific computing. Packt Pub. (2013)
- [7] Boffi, D., Brezzi, F., Fortin, M., et al.: Mixed finite element methods and applications, vol. 44. Springer (2013)
- [8] Boffi, D., Gastaldi, L.: A fictitious domain approach with Lagrange multiplier for fluid-structure interactions. *Numer. Math.* **135**(3), 711–732 (2016). <https://doi.org/10.1007/s00211-016-0814-1>
- [9] van Brummelen, E.H.: Added mass effects of compressible and incompressible flows in fluid-structure interaction. *J. Appl. Mech.* **03**, 021206–021207 (2009)

- [10] Bukač, M., Fu, G., Seboldt, A., Trenchea, C.: Time-adaptive partitioned method for fluid-structure interaction problems with thick structures. *J. Comput. Phys.* **473**, 111708 (2023)
- [11] Bukač, M., Trenchea, C.: Adaptive, second-order, unconditionally stable partitioned method for fluid-structure interaction. *Comput. Methods Appl. Mech. Eng.* **393**, 114847 (2022)
- [12] Burman, E., Fernández, M.A., Frei, S., Gerosa, F.M.: A mechanically consistent model for fluid-structure interactions with contact including seepage. *Comput. Methods Appl. Mech. Eng.* **392**, 114637 (2022)
- [13] Calderer, A., Guo, X., Shen, L., Sotiropoulos, F.: Coupled fluid-structure interaction simulation of floating offshore wind turbines and waves: a large eddy simulation approach. *J. Phys: Conf. Ser.* **524**, 012091 (2014). <https://doi.org/10.1088/1742-6596/524/1/012091>
- [14] Causin, P., Gerbeau, J.F., Nobile, F.: Added-mass effect in the design of partitioned algorithms for fluid-structure problems. *Comput. Methods Appl. Mech. Eng.* **194**(42), 4506–4527 (2005)
- [15] Chiang, C.Y., Pironneau, O., Sheu, T., Thiriet, M.: Numerical study of a 3D Eulerian monolithic formulation for incompressible fluid-structures systems. *Fluids* **2**(2), 34 (2017). <https://doi.org/10.3390/fluids2020034>
- [16] Dunne, T., Rannacher, R.: Adaptive finite element approximation of fluid-structure interaction based on an Eulerian variational formulation. In: *Lecture Notes in Computational Science and Engineering*, pp. 110–145. Springer Science Business Media (2006). https://doi.org/10.1007/3-540-34596-5_6
- [17] Finnegan, W., Goggins, J.: Numerical simulation of linear water waves and wave-structure interaction. *Ocean Eng.* **43**, 23–31 (2012)
- [18] Frei, S., Richter, T., Wick, T.: Locmodfe: locally modified finite elements for approximating interface problems in deal. ii. *Software Impacts* **8**, 100070 (2021)
- [19] Gazzola, F., Neustupa, J., Sperone, G.: On the planar Taylor-Couette system and related exterior problems. *arXiv preprint arXiv:2406.14960* (2024)
- [20] Haelterman, R., Bogaers, A.E., Scheufele, K., Uekermann, B., Mehl, M.: Improving the performance of the partitioned qn-ils procedure for fluid-structure interaction problems: filtering. *Comput. Struct.* **171**, 9–17 (2016)
- [21] Hecht, F.: New development in FreeFem++. *J. Numer. Math.* **20**(3–4), 251–265 (2012)
- [22] Hecht, F., Pironneau, O.: An energy stable monolithic Eulerian fluid-structure finite element method. *Int. J. Numer. Meth. Fluids* **85**(7), 430–446 (2017). <https://doi.org/10.1002/fld.4388>
- [23] Heil, M., Hazel, A.L., Boyle, J.: Solvers for large-displacement fluid-structure interaction problems: segregated versus monolithic approaches. *Comput. Mech.* **43**(1), 91–101 (2008). <https://doi.org/10.1007/s00466-008-0270-6>
- [24] Hessenthaler, A., Balmus, M., Röhrle, O., Nordsletten, D.: A class of analytic solutions for verification and convergence analysis of linear and nonlinear fluid-structure interaction algorithms. *Comput. Methods Appl. Mech. Eng.* **362**, 112841 (2020)
- [25] Hron, J., Turek, S.: A monolithic FEM/multigrid solver for an ALE formulation of fluid-structure interaction with applications in biomechanics. *Fluid-structure interaction* pp. 146–170 (2006)
- [26] Hübner, B., Walhorn, E., Dinkler, D.: A monolithic approach to fluid-structure interaction using space-time finite elements. *Comput. Methods Appl. Mech. Eng.* **193**(23–26), 2087–2104 (2004)
- [27] Li, Y., Castro, A., Sinokrot, T., Prescott, W., Carrica, P.: Coupled multi-body dynamics and CFD for wind turbine simulation including explicit wind turbulence. *Renew. Energy* **76**, 338–361 (2015)
- [28] Muddle, R.L., Mihajlović, M., Heil, M.: An efficient preconditioner for monolithically-coupled large-displacement fluid-structure interaction problems with pseudo-solid mesh updates. *J. Comput. Phys.* **231**(21), 7315–7334 (2012). <https://doi.org/10.1016/j.jcp.2012.07.001>
- [29] Naseri, A., Totounferoush, A., González, I., Mehl, M., Pérez-Segarra, C.D.: A scalable framework for the partitioned solution of fluid-structure interaction problems. *Comput. Mech.* **66**, 471–489 (2020)
- [30] Rall, L.B.: Nonlinear functional analysis and applications: proceedings of an advanced seminar conducted by the Mathematics Research Center, the University of Wisconsin, Madison, October 12–14, 1970. 26. Elsevier (2014)
- [31] Rannacher, R., Richter, T.: An adaptive finite element method for fluid-structure interaction problems based on a fully Eulerian formulation. In: *Fluid-Structure Interaction II*, pp. 159–191. Springer Berlin Heidelberg (2010). https://doi.org/10.1007/978-3-642-14206-2_7
- [32] Richter, T.: A fully Eulerian formulation for fluid-structure-interaction problems. *J. Comput. Phys.* **233**, 227–240 (2013). <https://doi.org/10.1016/j.jcp.2012.08.047>
- [33] Spenke, T., Hosters, N., Behr, M.: A multi-vector interface quasi-Newton method with linear complexity for partitioned fluid-structure interaction. *Comput. Methods Appl. Mech. Eng.* **361**, 112810 (2020)
- [34] Taylor, G.I.: Viii. stability of a viscous liquid contained between two rotating cylinders. *Phil. Trans. R. Soc. London Ser. A-Contain. Pap. Math. Phys. Character* **223**(605–615), 289–343 (1923)
- [35] Wall, W.A., Gerstenberger, A., Gamnitzer, P., Forster, C., Ramm, E.: Large deformation fluid-structure interaction—advances in ALE methods and new fixed grid approaches. *Lect. Notes Comput. Sci. Eng.* **53**, 195 (2006)
- [36] Wang, Y., Jimack, P.K., Walkley, M.A.: A one-field monolithic fictitious domain method for fluid-structure interactions. *Comput. Methods Appl. Mech. Eng.* **317**, 1146–1168 (2017). <https://doi.org/10.1016/j.cma.2017.01.023>
- [37] Wang, Y., Jimack, P.K., Walkley, M.A.: Energy analysis for the one-field fictitious domain method for fluid-structure interactions. *Appl. Numer. Math.* **140**, 165–182 (2019). <https://doi.org/10.1016/j.apnum.2019.02.003>
- [38] Wang, Y., Jimack, P.K., Walkley, M.A.: A theoretical and numerical investigation of a family of immersed finite element methods. *J. Fluids Struct.* **91**, 102754 (2019)

- [39] Wang, Y., Jimack, P.K., Walkley, M.A., Pironneau, O.: An energy stable one-field monolithic arbitrary Lagrangian-Eulerian formulation for fluid-structure interaction. *J. Fluids Struct.* **98**, 103117 (2020). <https://doi.org/10.1016/j.jfluidstructs.2020.103117>
- [40] Wendl, M.C.: General solution for the couette flow profile. *Phys. Rev. E* **60**(5), 6192 (1999)
- [41] Wick, T.: Coupling of fully Eulerian and arbitrary Lagrangian-Eulerian methods for fluid-structure interaction computations. *Comput. Mech.* **52**(5), 1113–1124 (2013). <https://doi.org/10.1007/s00466-013-0866-3>
- [42] Womersley, J.R.: Method for the calculation of velocity, rate of flow and viscous drag in arteries when the pressure gradient is known. *J. Physiol.* **127**(3), 553 (1955)
- [43] Yamada, T., Hong, G., Kataoka, S., Yoshimura, S.: Parallel partitioned coupling analysis system for large-scale incompressible viscous fluid-structure interaction problems. *Comput. Fluids* **141**, 259–268 (2016)

Yongxing Wang
School of Computer Science
University of Leeds
Leeds
UK
e-mail: scsywan@leeds.ac.uk

Olivier Pironneau
LJLL
Sorbonne University
Paris
France
e-mail: olivier.pironneau@upmc.fr

(accepted: December 26, 2025)